INTERNATIONAL JOURNAL FOR NUMERICAL METHODS IN FLUIDS
Int. J. Numer. Meth. Fluids 2011; **67**:109–134
Published online 6 May 2010 in Wiley Online Library (wileyonlinelibrary.com). DOI: 10.1002/fld.2344

Development of level set method with good area preservation to predict interface in two-phase flows

Tony W. H. Sheu[1,2,3,*,†], C. H. Yu[1] and P. H. Chiu[1]

[1]*Department of Engineering Science and Ocean Engineering, National Taiwan University, No. 1, Sec. 4, Roosevelt Road, Taipei, Taiwan*
[2]*Taida Institute of Mathematical Sciences (TIMS), National Taiwan University, Taipei, Taiwan*
[3]*Center for Quantum Science and Engineering (CQSE), National Taiwan University, Taipei, Taiwan*

SUMMARY

A two-step conservative level set method is proposed in this study to simulate the gas/water two-phase flow. For the sake of accuracy, the spatial derivative terms in the equations of motion for an incompressible fluid flow are approximated by the coupled compact scheme. For accurately predicting the modified level set function, the dispersion-relation-preserving advection scheme is developed to preserve the theoretical dispersion relation for the first-order derivative terms shown in the pure advection equation cast in conservative form. For the purpose of retaining its long-time accurate Casimir functionals and Hamiltonian in the transport equation for the level set function, the time derivative term is discretized by the sixth-order accurate symplectic Runge–Kutta scheme. To resolve contact discontinuity oscillations near interface, nonlinear compression flux term and artificial damping term are properly added to the second-step equation of the modified level set method. For the verification of the proposed dispersion-relation-preserving scheme applied in non-staggered grids for solving the incompressible flow equations, three benchmark problems have been chosen in this study. The conservative level set method with area-preserving property proposed for capturing the interface in incompressible fluid flows is also verified by solving the dam-break, Rayleigh–Taylor instability, bubble rising in water, and droplet falling in water problems. Good agreements with the referenced solutions are demonstrated in all the investigated problems. Copyright © 2010 John Wiley & Sons, Ltd.

Received 5 November 2009; Revised 25 March 2010; Accepted 26 March 2010

KEY WORDS: conservative level set method; coupled compact scheme; dispersion-relation-preserving; Casimir; Hamiltonian; sixth-order accurate; symplectic Runge–Kutta; area preservation

1. INTRODUCTION

Interface between different phases, where surface tension in the flow plays a key role in affecting its phenomenal behavior, is commonly found in some areas of practical importance and scientific significance. Typical problems include etching, deposition, lithography, image processing and crystal growth [1]. Study of the complex phenomena in air–water interfacial dynamics, breaking surface wave, solidification–melt dynamics, two-phase reacting flow, and flow–structure

*Correspondence to: Tony W. H. Sheu, Department of Engineering Science and Ocean Engineering, National Taiwan University, No. 1, Sec. 4, Roosevelt Road, Taipei, Taiwan.
†E-mail: twhsheu@ntu.edu.tw

Contract/grant sponsor: National Science Council of Republic of China; contract/grant numbers: NSC-94-2611-E-002-021, NSC-94-2745-P-002-002
Contract/grant sponsor: CQSE project; contract/grant number: 97R0066-69

interactions involves determining the temporal surface advancement driven by the carrier flow under different physical loadings. The necessity of capturing or tracking time-evolving interface with possible sharply varying topology and front propagation speed can make the numerical analysis of the differential equations for their respective two-phase fluid flows an even challenging topic. Two classes of methods, which are known as the interface tracking and interface capturing methods, are in common use. Interface tracking methods, which employ a deforming mesh that conforms to the interface, are developed in Lagrangian sense. The mesh, as a result, should explicitly represent the interface. Interface capturing methods are, on the contrary, belong to the Eulerian type since interface itself is an implicit function defined on a fixed mesh. In this study, our attention will be concentrated on the modified level set method, applied together with the incompressible flow solver in non-staggered grids, to predict the air/water interface, where surface tension needs to be taken into account.

The most common numerical methods that have been applied to predict the air/water interface include the vortex method [2], boundary integral method [3], volume of fluid (VoF) method [4], front tracking method [5], and phase field method [6–8]. One can also combine the level set and projection methods to avoid an explicit interface tracking [9]. There exist some advantages and disadvantages of applying these interface capturing methods and it is difficult to conclude that one method is generally superior to the others. Arbitrary Lagrangian Eulerian [10] and Marker and Cell [11] methods are the two commonly applied interface tracking methods, which have been known to be very efficient in modeling a small interface deformation. For the interface undergoing a large deformation, a fairly expensive re-meshing procedure is needed. If surface tension needs to be considered in the simulation of incompressible two-phase flows, the VoF and level set methods are most commonly referred to.

After the pioneering work of Osher and Sethian [12], progress towards refining the level set method has made this method a good candidate to simulate the fluid flows that involve moving interfaces. Owing to the smooth nature of the level set function, across the interface both of the interface and its curvature can be easily transported and accurately calculated, respectively. A signed distance function for the sake of re-shaping the level set function and a reinitialization procedure for the purpose of enhancing numerical stability are normally required in the development of traditional level set methods [13]. Owing to the lack of geometric conservative law [14, 15], there is no guarantee that the employed reinitialization process can preserve either flow volume or area in time. In each time step, fluid mass of a small quantity may, therefore, be lost or gained. As time proceeds, even a negligibly small error can be accumulated to a sufficiently large magnitude and may, finally, lead the solution to breakdown in the prediction of flow equations under the incompressible constraint condition (or conservation of mass). To overcome the problem resulting from the level set methods, the particle level set method [16], level set method with mass correction procedure [17], coupled level set and VoF method [18], and adaptive tree method [19] have been proposed. For the details of level set methods, one can refer to the excellent review books of Osher and Fedkiw [20] and Sethian [21]. A modified level set method with a built-in conservative (or area-preserving) property will be developed in the current incompressible flow simulation with the goal to preserve mass [22].

The outline of this paper is as follows. In Section 2, the differential equations governing the motion of two incompressible fluids will be presented. Section 3 describes the conservative level set method, which involves solving the nonlinear transport equation in two steps. In Section 4, the coupled compact scheme accommodating the dispersion-relation-preserving property will be employed to model the advected interface. Regularized incompressible viscous flow solver, which is developed in non-staggered grids, is also presented to solve the primitive variables explicitly. While very accurate, stable, and efficient advection schemes have been proposed in the literature and they can be applied to solve the pure advection equation, which governs the transport of level set function, none of them have taken the area-preservation property into account [23]. Since the area of fluids within each contour of the level-set function is preserved in the divergence-free flow field, we present in section 5 the implicit symplectic-type temporal scheme to solve the pure advection equation, which appears in the first step of the modified level set method.

DOI: 10.1002/fld

The approximation scheme chosen for the first-order spatial derivative term accommodating the dispersion relation is also presented. Section 6 is presented to justify the analysis code by solving the pure convection equation subjected to a sharply varying initial condition and the Navier–Stokes problem with the benchmark solution for the carrier fluid flow. Section 7 presents the predicted results for the dam-break, Rayleigh–Taylor instability, bubble rising, and liquid droplet falling problems. Finally, we will draw some conclusions in Section 8.

2. GOVERNING EQUATIONS

For the two immiscible fluids under current investigation, liquid and gas are both assumed to be incompressible. The resulting equations of motion for these two fluids in a gravitational vector field $\underline{g}$ can be represented by the following incompressible Navier–Stokes equations:

$$\frac{\mathrm{D}\underline{u}}{\mathrm{D}t}=\frac{1}{\rho}[-\nabla p+\nabla\cdot(2\mu\underline{\underline{\mathbf{D}}})-\underline{T}+\rho\underline{g}] \tag{1}$$

$$\nabla\cdot\underline{u}=0 \tag{2}$$

where $\mathrm{D}\underline{u}/\mathrm{D}t(\equiv(\partial\underline{u}/\partial t)+(\underline{u}\cdot\nabla)\underline{u})$ is the material derivative of velocity vector $\underline{u}$. Two physical properties ρ and μ, which are varied with time and space, represent the fluid density and viscosity, respectively. The tensor $\underline{\underline{\mathbf{D}}}$ shown above with the components given by $D_{ij}=\frac{1}{2}(u_{i,j}+u_{j,i})$ denotes the rate of deformation.

In addition to the stress tensor $-p\underline{\underline{\mathbf{I}}}+2\mu\underline{\underline{\mathbf{D}}}$, where $\underline{\underline{\mathbf{I}}}$ is the identity matrix, the other surface tension vector $\underline{T}$ per unit interfacial area concentrated solely on the two-fluid interface is given below

$$\underline{T}=\sigma\kappa\delta\underline{n} \tag{3}$$

In the above, δ is the Dirac delta function, σ is denoted as the surface tension coefficient, and κ is the curvature of time-evolving interface. The unit outward normal vector $\underline{n}$ along the interface is pointed to the surrounding liquid. One can then express the unit normal and the curvature of interface in terms of the phase field function ϕ, respectively, as

$$\underline{n}=\frac{\nabla\phi}{|\nabla\phi|}\quad\text{and}\quad\kappa=\nabla\cdot\frac{\nabla\phi}{|\nabla\phi|}$$

The need that Equations (1)–(2) should be solved within the framework of level set method is enlightened.

Take $u_\mathrm{r}, l_\mathrm{r}, t_\mathrm{r}, p_\mathrm{r}(\equiv\rho_\mathrm{r}g l_\mathrm{r}), \rho_\mathrm{r}, \mu_\mathrm{r}$ as the referenced values for the respective velocity, length, time, pressure, density, and viscosity, the normalized (or dimensionless) continuity equation remains unchanged. The other dimensionless vector equation for conserving the momentum components can be formulated as

$$\underline{u}_t+(\underline{u}\cdot\nabla)\underline{u}=\frac{1}{\rho}\left[-\nabla p+\frac{1}{Re}\nabla\cdot(2\mu\underline{\underline{\mathbf{D}}})-\frac{1}{We}\kappa(\phi)\delta(\phi)\nabla\phi\right]+\frac{1}{Fr^2}\underline{e}_g \tag{4}$$

where $\underline{e}_g$ denotes the unit gravitational vector and the Reynolds number is given by $Re=\rho_\mathrm{r}u_\mathrm{r}l_\mathrm{r}/\mu_\mathrm{r}$. Another characteristic parameter We shown above is known as the Weber number, which is defined as $We=\rho_\mathrm{r}u_\mathrm{r}^2l_\mathrm{r}/\sigma$. Both of the fluid density and viscosity will be smoothly approximated by $\rho=\rho_1+(\rho_2-\rho_1)\phi$ and $\mu=\mu_1+(\mu_2-\mu_1)\phi$, where ρ_i and μ_i $(i=1,2)$ are the dimensionless densities and viscosities of the two investigated fluids, respectively.

3. TWO-STEP INTERFACE CAPTURING SOLUTION ALGORITHM

For the two investigated immiscible fluids, both ρ and μ are assumed to be uniform all the time in their respective phases, implying that $(\mathrm{D}\rho/\mathrm{D}t)=(\mathrm{D}\mu/\mathrm{D}t)=0$. In other words, the transport

DOI: 10.1002/fld

equations for the fluid density and viscosity depend only on the flow velocity $\underline{u}$ by means of $\rho_t+(\underline{u}\cdot\nabla)\rho=0$ and $\mu_t+(\underline{u}\cdot\nabla)\mu=0$. Across an interface there exists, however, an abrupt change in the magnitudes of ρ and μ. The air/water interface, denoted by the level set function ϕ, will be advected in a fluid flow following the linear advection equation given by:

$$\phi_t+\underline{u}\cdot\nabla\phi=0 \tag{5}$$

It is noted that the magnitude of ϕ across the interface has a sharp change from zero to one. The interface is represented by the contour value of $\phi=0.5$ which is suggested by Olsson and Kreiss [22] for getting a better volume conservation. To avoid numerical instabilities near the interface, Equation (5) will be further transformed to its equivalent conservative form given below by taking into account the fact that the velocity vector $\underline{u}$ under current investigation is always divergence-free

$$\phi_t+\nabla\cdot(\underline{u}\phi)=0 \tag{6}$$

Over each time step Δt, ϕ will be first computed from the pure advection equation $\phi_t+\nabla\cdot(\underline{u}\phi)=0$, which is normally employed in the traditional level set method to advect the level set function ϕ. The solution of ϕ computed from Equation (6) is then employed as the initial solution to solve the following nonlinear equation for purposes of enhancing numerical stability and enabling compression of the solution across interface [22]:

$$\phi_\tau+\nabla\cdot[\phi(1-\phi)\underline{n}]=\overline{\mu}\nabla\cdot(\nabla\phi) \tag{7}$$

Note that the employment of the explicitly added nonlinear flux term, which is $\phi(1-\phi)\underline{n}$, in the above equation helps to compress the solution and this addition can, thus, resolve the contact surface. Furthermore, the artificial damping term is introduced into the current formulation to damp out the numerical oscillations generated by the discontinuities in the vicinity of interface. Note that the introduced damping mechanism for resolving oscillations near interface may deteriorate the mass conservation.

In the present calculation of Equation (7), the time increment is chosen as $\Delta\tau=0.1\Delta t$. As a criterion of examining whether or not the time accurate solution has been computed, we use $|\phi^{m+1}-\phi^m|<\text{TOL}$ where TOL is the problem-dependent specified tolerance. In practice, only few iterations are needed for all the computations carried out in this study. Besides, the value of $\overline{\mu}$ will be chosen as $1.1\Delta x$ in all calculations.

4. INCOMPRESSIBLE FLOW SOLVER IN NON-STAGGERED GRIDS

4.1. Dispersion-relation-preserving coupled compact scheme for the spatial derivative terms in momentum equations

The first-order derivative term $\partial u/\partial x$ and the second-order derivative term $\partial^2 u/\partial x^2$, for example, will be approximated in the three-point grid stencil by the following compact scheme:

$$a_1\left.\frac{\partial u}{\partial x}\right|_{i-1}+\left.\frac{\partial u}{\partial x}\right|_i=\frac{1}{h}(c_1u_{i-1}+c_2u_i+c_3u_{i+1})$$
$$-h\left(b_1\left.\frac{\partial^2 u}{\partial x^2}\right|_{i-1}+b_2\left.\frac{\partial^2 u}{\partial x^2}\right|_i+b_3\left.\frac{\partial^2 u}{\partial x^2}\right|_{i+1}\right) \tag{8}$$

$$\overline{b}_1\left.\frac{\partial^2 u}{\partial x^2}\right|_{i-1}+\left.\frac{\partial^2 u}{\partial x^2}\right|_i+\overline{b}_3\left.\frac{\partial^2 u}{\partial x^2}\right|_{i+1}=\frac{1}{h^2}(\overline{c}_1u_{i-1}+\overline{c}_2u_i+\overline{c}_3u_{i+1})$$
$$-\frac{1}{h}\left(\overline{a}_1\left.\frac{\partial u}{\partial x}\right|_{i-1}+\overline{a}_2\left.\frac{\partial u}{\partial x}\right|_i+\overline{a}_3\left.\frac{\partial u}{\partial x}\right|_{i+1}\right) \tag{9}$$

DOI: 10.1002/fld

As for the terms $\partial u/\partial y$ and $\partial^2 u/\partial y^2$ along the y-direction, they can be similarly approximated as $\partial u/\partial x$ and $\partial^2 u/\partial x^2$. Note that the compact schemes for $(\partial u/\partial x)|_i$ and $(\partial^2 u/\partial x^2)|_i$ are coupled through $(\partial u/\partial x)|_{i-1}$, $(\partial u/\partial x)|_i$, $(\partial u/\partial x)|_{i+1}$, $(\partial^2 u/\partial x^2)|_{i-1}$, $(\partial^2 u/\partial x^2)|_i$, $(\partial^2 u/\partial x^2)|_{i+1}$, u_{i-1}, u_i, u_{i+1}. For the sake of description, only the case involving the positive convective coefficient will be considered. For the case with the negative convective coefficient, the derivation will be the same.

Approximation of $\partial^2 u/\partial x^2$ normally introduces dissipative error. Owing to this physical reason, the weighting coefficients shown in Equation (9) will be determined solely from the modified equation analysis for getting a higher solution accuracy. Along the line of this thought, we can derive the coefficients in Equation (9) as $\overline{a}_1=-\frac{9}{8}, \overline{a}_2=0, \overline{a}_3=\frac{9}{8}, \overline{b}_1=-\frac{1}{8}, \overline{b}_3=-\frac{1}{8}, \overline{c}_1=3, \overline{c}_2=-6$, and $\overline{c}_3=3$. Note that these derived coefficients shown in Equation (9) have the same values as those given in Chu and Fan [24]. It is remarkable to point out here that the use of these derived coefficients for $\partial^2 u/\partial x^2$ can render the following modified equation, from which the spatial accuracy order is known to be sixth in a grid involving only three nodal points

$$\frac{\partial^2 u}{\partial x^2}=\left.\frac{\partial^2 u}{\partial x^2}\right|_{\text{exact}}+\frac{h^6}{20\,160}\frac{\partial^8 u}{\partial x^8}+\frac{h^8}{604\,800}\frac{\partial^{10} u}{\partial x^{10}}+O(h^{12})+\cdots$$

For the coefficients $a_1, b_1\sim b_3, c_1\sim c_3$, they are partly determined by applying the Taylor series expansions for $u_{i\pm1}$, $(\partial u/\partial x)|_{i-1}$ and $(\partial^2 u/\partial x^2)|_{i\pm1}$ with respect to u_i, $(\partial u/\partial x)|_i$ and $(\partial^2 u/\partial x^2)|_i$. This is followed by eliminating the leading error terms derived in the modified equation, from which the following set of algebraic equations for Equation (8) can be derived

$$c_1+c_2+c_3=0 \tag{10}$$

$$-a_1-c_1+c_3-1=0 \tag{11}$$

$$-a_1+b_1+b_2+b_3-\frac{c_1}{2}-\frac{c_3}{2}=0 \tag{12}$$

$$\frac{a_1}{2}-b_1+b_3+\frac{c_1}{6}-\frac{c_3}{6}=0 \tag{13}$$

$$-\frac{a_1}{6}+\frac{b_1}{2}+\frac{b_3}{2}-\frac{c_1}{24}-\frac{c_3}{24}=0 \tag{14}$$

$$\frac{a_1}{24}-\frac{b_1}{6}+\frac{b_3}{6}+\frac{c_1}{120}-\frac{c_3}{120}=0 \tag{15}$$

One more algebraic equation is in need to uniquely determine the seven introduced coefficients shown in Equation (8).

For accurately approximating the first-order derivative term from Equation (8), it is legitimate to preserve the dispersive nature embedded in $\partial u/\partial x$ as best as one can since dispersion relation defines the relation between the angular frequency and the wavenumber of the first-order dispersive term [25]. In other words, the solution can be accurately calculated provided that the dispersion relation is well preserved. It is therefore important for us to develop a scheme which accommodates the dispersion relation for the first-order spatial derivative term.

The Fourier transform and its inverse of u given below will be employed to preserve the dispersion relation

$$\tilde{u}(\alpha)=\frac{1}{2\pi}\int_{-\infty}^{+\infty}u(x)\exp(-\mathbf{i}\alpha x)\mathrm{d}x \tag{16}$$

$$u(x)=\int_{-\infty}^{+\infty}\tilde{u}(\alpha)\exp(\mathbf{i}\alpha x)\mathrm{d}\alpha \tag{17}$$

where the notation $\mathbf{i}$ shown above is equal to $\sqrt{-1}$. Development of the proposed dispersion-relation-preserving scheme is followed by performing the Fourier transform on each term shown

DOI: 10.1002/fld

in Equations (8) and (9). The actual wavenumber α for Equations (8) and (9) can therefore be derived as

$$\mathbf{i}\alpha h(a_1\exp(-\mathbf{i}\alpha h)+1)\simeq c_1\exp(-\mathbf{i}\alpha h)+c_2+c_3\exp(\mathbf{i}\alpha h)-(\mathbf{i}\alpha h)^2(b_1\exp(-\mathbf{i}\alpha h)+b_2 +b_3\exp(\mathbf{i}\alpha h)) \tag{18}$$

and

$$(\mathbf{i}\alpha h)^2(-\tfrac{1}{8}\exp(-\mathbf{i}\alpha h)+1-\tfrac{1}{8}\exp(\mathbf{i}\alpha h))\simeq 3\exp(-\mathbf{i}\alpha h)-6+3\exp(\mathbf{i}\alpha h) -\mathbf{i}\alpha h(-\tfrac{8}{9}\exp(-\mathbf{i}\alpha h)+\tfrac{8}{9}\exp(\mathbf{i}\alpha h)) \tag{19}$$

Thanks to the above two equations, the effective wavenumbers α' and α'' will be derived to get the same expressions as those shown in the right-hand sides of Equations (18) and (19) [25]. We are then led to get α' and α'' as follows:

$$\mathbf{i}\alpha' h(a_1\exp(-\mathbf{i}\alpha h)+1)=c_1\exp(-\mathbf{i}\alpha h)+c_2+c_3\exp(\mathbf{i}\alpha h)-(\mathbf{i}\alpha'' h)^2(b_1\exp(-\mathbf{i}\alpha h)+b_2 +b_3\exp(\mathbf{i}\alpha h)) \tag{20}$$

$$\mathbf{i}\alpha' h(-\tfrac{8}{9}\exp(-\mathbf{i}\alpha h)+\tfrac{8}{9}\exp(\mathbf{i}\alpha h))=3\exp(-\mathbf{i}\alpha h)-6+3\exp(\mathbf{i}\alpha h)-(\mathbf{i}\alpha'' h)^2(-\tfrac{1}{8}\exp(-\mathbf{i}\alpha h)+1 -\tfrac{1}{8}\exp(\mathbf{i}\alpha h)) \tag{21}$$

The expressions given below for α' and α'' can be derived by solving Equations (20) and (21) simultaneously

$$\begin{aligned}\alpha' h=&-\mathbf{i}(24b_1\exp(-2\mathbf{i}\alpha h)+c_1\exp(-2\mathbf{i}\alpha h)+c_3+c_1+24b_1+c_2\exp(-\mathbf{i}\alpha h)\\ &+24b_2\exp(-\mathbf{i}\alpha h)+24b_3-48b_1\exp(-\mathbf{i}\alpha h)-8c_1\exp(-\mathbf{i}\alpha h)\\ &-48b_3\exp(\mathbf{i}\alpha h)+24b_2\exp(\mathbf{i}\alpha h)+24b_3\exp(2\mathbf{i}\alpha h)-48b_2\\ &+c_2\exp(\mathbf{i}\alpha h)+c_3\exp(2\mathbf{i}\alpha h)-8c_3\exp(\mathbf{i}\alpha h)-8c_2)/\\ &(-8+\exp(\mathbf{i}\alpha h)-8a_1\exp(-\mathbf{i}\alpha h)+a_1\exp(-2\mathbf{i}\alpha h)-9b_1\exp(-2\mathbf{i}\alpha h)\\ &-9b_2\exp(-\mathbf{i}\alpha h)+9b_2\exp(\mathbf{i}\alpha h)+9b_3\exp(2\mathbf{i}\alpha h)+a_1+9b_1-9b_3+\exp(\mathbf{i}\alpha h))\end{aligned} \tag{22}$$

$$\alpha'' h=\sqrt{-\frac{3\exp(-\mathbf{i}\alpha h)-6+3\exp(\mathbf{i}\alpha h)-\mathbf{i}\alpha' h(-\frac{8}{9}\exp(-\mathbf{i}\alpha h)+\frac{8}{9}\exp(\mathbf{i}\alpha h))}{-\frac{1}{8}\exp(-\mathbf{i}\alpha h)+1-\frac{1}{8}\exp(\mathbf{i}\alpha h)}} \tag{23}$$

To get a better dispersive accuracy for α', it is demanded that $\alpha h\approx\Re(\alpha' h)$, where $\Re(\alpha' h)$ denotes the real part of $\alpha' h$. This implies that $E(\alpha)$ defined below should be a small value of positive sign

$$E(\alpha)=\int_{-\pi/2}^{\pi/2}[W(\alpha h-\Re(\alpha' h))]^2\mathrm{d}(\alpha h)=\int_{-\pi/2}^{\pi/2}[W(\gamma-\Re(\gamma'))]^2\mathrm{d}\gamma \tag{24}$$

where $\gamma=\alpha h$ and $\gamma'=\alpha' h$. Note that Equation (24) is analytically integrable provided that the weighting function W shown above is chosen as:

$$\begin{aligned}W=&-16+72b_3+72b_1-81b_1^2-81b_3^2-81b_2^2-162b_2b_3\cos(\gamma)-144a_1b_3\cos(\gamma)-162b_1b_2\cos(\gamma)\\ &-a_1^2\cos(\gamma)^2+8a_1^2\cos(\gamma)-18b_3\cos(\gamma)^3+18b_1\cos(\gamma)^3+81b_2^2\cos(\gamma)^2+162b_1b_3-72b_1\cos(\gamma)^2\\ &+81b_3^2\cos(\gamma)^2+81b_1^2\cos(\gamma)^2-72a_1b_2-18b_1\cos(\gamma)+16a_1\cos(\gamma)^2-2a_1\cos(\gamma)^3\\ &+72b_3\cos(\gamma)^2+18b_3\cos(\gamma)-32a_1\cos(\gamma)-36a_1b_3\cos(\gamma)^4-18a_1b_2\cos(\gamma)^3+162b_2b_3\cos(\gamma)^3\\ &+162b_1b_2\cos(\gamma)^3+324b_1b_3\cos(\gamma)^4+72a_1b_2\cos(\gamma)^2+144a_1b_3\cos(\gamma)^3-486b_1b_3\cos(\gamma)^2\\ &+36a_1b_3\cos(\gamma)^2+18a_1b_2\cos(\gamma)+8\cos(\gamma)-16a_1^2-\cos(\gamma)^2\end{aligned} \tag{25}$$

DOI: 10.1002/fld

Note that the integration interval shown in Equation (24) should be sufficiently large and can, as a result, take a complete period of sine (or cosine) wave into account.

To make E defined in Equation (24) a positive and minimum value, the following extreme condition is enforced

$$\frac{\partial E}{\partial c_3}=0 \tag{26}$$

The above equation, which is employed to preserve the dispersion relation, will be solved together with the six previously derived algebraic equations, by virtue of the modified equation analysis to retain a smaller dissipation error as well as an improved dispersion accuracy. The seven introduced unknowns can then be uniquely determined as $a_1=0.875$, $b_1=0.125128234160$, $b_2=-0.24871765840$, $b_3=0.000128234160$, $c_1=-1.935961190081$, $c_2=1.9969223801622$ and $c_3=-0.0609611900811$. Given these coefficients, the resulting upwinding scheme for $\partial u/\partial x$ can be shown to have the spatial accuracy order of fifth according to the derived modified equation given below

$$\frac{\partial u}{\partial x}=\frac{\partial u}{\partial x}\bigg|_{\text{exact}}-0.00070085615243989224 75h^5\frac{\partial^6 u}{\partial x^6}+0.00019841269841269841 27h^6\frac{\partial^7 u}{\partial x^7}$$
$$-0.00004988305074583303 90h^7\frac{\partial^8 u}{\partial x^8}+O(h^8)+\cdots \tag{27}$$

4.2. Solution algorithm

Thanks to the Helmholtz–Hodge decomposition theorem [26], the vector field $\underline{u}$ for Equation (1) can be decomposed into the zero-curl and zero-divergence two components. The intermediate velocity $\underline{u}^{n+1/2}$ can then be calculated from the fully implicit equation along with the prescribed velocity vector $\underline{u}^{n+1/2}|_{\partial\Omega}(\equiv\underline{b})$ along the boundary $\partial\Omega$ for the following Navier–Stokes equations written in the vector form

$$\frac{\underline{u}^{n+1/2}-\underline{u}^n}{\Delta t}=-(\underline{u}^{n+1/2}\cdot\nabla)\underline{u}^{n+1/2}+\frac{1}{\rho Re}\nabla\cdot(2\mu\mathbf{D}^{n+1/2})+\underline{f}^{n+1} \tag{28}$$

where $\underline{f}$ is expressed as $-(1/\rho)(1/We)\kappa(\phi)\delta\nabla\phi+1/Fr^2\underline{e}_g$. Note that the pressure variable has been eliminated from the momentum equations. Analysis of the incompressible viscous flow equations becomes thus much simplified.

The above equation can be solved sequentially from the advection step, given by

$$\frac{\underline{u}_a^{n+1/2}-\underline{u}^n}{\Delta t}+(\underline{u}^n\cdot\nabla)\underline{u}^n=0$$

and the diffusion step, given by

$$\frac{\underline{u}^{n+1/2}-\underline{u}_a^{n+1/2}}{\Delta t}=\frac{1}{\rho Re}\nabla\cdot(2\mu\mathbf{D}^{n+1/2})+\underline{f}^{n+1/2}$$

The intermediate velocity solution $\underline{u}^{n+1/2}$ calculated from the above two steps does not necessarily satisfy the divergence-free constraint condition. As a result, the intermediate vector $\underline{u}^{n+1/2}$ is decomposed into the sum of the solenoidal velocity $\underline{u}^{n+1}$ and the gradient of the currently chosen scalar function, which is proportional to $\Delta t\nabla p^{n+1}$. The integrity of employing the following two equations in the projection step is enlightened:

$$\frac{\underline{u}^{n+1}-\underline{u}^{n+1/2}}{\Delta t}=-\frac{\nabla p^{n+1}}{\rho} \tag{29}$$

DOI: 10.1002/fld

$$\nabla \cdot \underline{u}^{n+1} = 0 \tag{30}$$

According to Equation (29), the calculation of $\underline{u}^{n+1}$ needs a pressure solution. By applying the divergence operator to both hand sides of $\underline{u} = \underline{w} - \nabla p$, the Poisson equation given by $\nabla \cdot \nabla p/\rho = \nabla \cdot \underline{u}^{n+1/2}$ can be derived.

There exists a necessity of specifying the pressure boundary value in this formulation. However, in theory pressure boundary value needs not to be specified when solving the primitive-variable Navier–Stokes equations. In addition, analysis of the Poisson equation for p is normally expensive. For these two reasons, the regularization method will be adopted. Development of the regularization method for $(\partial \underline{u}/\partial \underline{t}) + (\underline{u} \cdot \nabla)\underline{u} = -(\nabla p/\rho) + (1/Re)\nabla^2 \underline{u} + \underline{f}$ starts with substituting

$$\frac{\underline{u}^{n+1} - \underline{u}^{n+1/2}}{\Delta t} = -\frac{\nabla p}{\rho}^{n+1}$$

(or Equation (29)) into the semi-discretized momentum equation given below

$$\frac{\underline{u}^{n+1} - \underline{u}^{n}}{\Delta t} + (\underline{u}^* \cdot \nabla)\underline{u}^* - \frac{1}{\rho Re}\nabla^2 \underline{u}^* + \frac{\nabla p}{\rho}^* = -\frac{\nabla p'}{\rho} + M_1 + M_2 - \underline{f}^{n+1} \tag{31}$$

where '*' denotes the most updated value. In the above, $M_1 = [(\underline{u}^* \cdot \nabla)(\nabla p/\rho)' + ((\nabla p/\rho)' \cdot \nabla)\underline{u}^*]\Delta t - (1/\rho Re)\nabla(\nabla \cdot \underline{u}^*)$, $M_2 = -[((\nabla p/\rho)' \cdot \nabla)\nabla p/\rho']\Delta t^2$ and [27]

$$p'_{i,j} = p'^*_{i,j} + \left(\frac{p'^*_{i-1,j}}{\rho_{i-1/2}\Delta x^2} + \frac{p'^*_{i+1,j}}{\rho_{i+1/2}\Delta x^2} + \frac{p'^*_{i,j-1}}{\rho_{j-1/2}\Delta x^2} + \frac{p'^*_{i,j-1}}{\rho_{j-1/2}\Delta x^2} \right) \Bigg/ \left(\frac{1}{\rho_{i+1/2}\Delta x^2} + \frac{1}{\rho_{i-1/2}\Delta x^2} + \frac{1}{\rho_{j+1/2}\Delta y^2} + \frac{1}{\rho_{j-1/2}\Delta y^2} \right)$$

5. NUMERICAL SCHEME FOR THE MODIFIED LEVEL SET EQUATION

5.1. Dispersion-relation-preserving compact scheme for the advection term

It has been well known that the convective flux term shown in Equation (6) is recommended to be approximated in conservative form for the sake of enhancing scheme stability. The guideline behind approximating $(\partial(u\phi)/\partial x)|_i$, for example, is to conserve the flux term $u\phi$ across a cell of length h by means of

$$\left.\frac{\partial(u\phi)}{\partial x}\right|_i = \frac{u_{i+1/2}\phi_{i+1/2} - u_{i-1/2}\phi_{i-1/2}}{h} \tag{32}$$

Define first the values of ϕ at the half nodal points $i \pm \frac{1}{2}$ as follows:

$$\phi_{i+1/2} = \gamma_1 \phi_i + \gamma_2 \phi_{i+1} - \left(\alpha_1 \phi_{i-1/2} + h \left(\beta_1 \left.\frac{\partial \phi}{\partial x}\right|_{i-1/2} + \beta_2 \left.\frac{\partial \phi}{\partial x}\right|_{i+1/2} + \beta_3 \left.\frac{\partial \phi}{\partial x}\right|_{i+\frac{3}{2}} \right) \right) \tag{33}$$

and

$$\phi_{i-1/2} = \gamma_1 \phi_{i-1} + \gamma_2 \phi_i - \left(\alpha_1 \phi_{i-3/2} + h \left(\beta_1 \left.\frac{\partial \phi}{\partial x}\right|_{i-3/2} + \beta_2 \left.\frac{\partial \phi}{\partial x}\right|_{i-1/2} + \beta_3 \left.\frac{\partial \phi}{\partial x}\right|_{i+1/2} \right) \right) \tag{34}$$

DOI: 10.1002/fld

One can then substitute them into $(\partial\phi/\partial x)|_i=(\phi_{i+1/2}-\phi_{i-1/2})/h$ to get the algebraic equation for $\partial\phi/\partial x$ at the node i. Derivation of α_i, β_i and γ_i is then followed by comparing the coefficients derived in Section 4.1 for $(\partial\phi/\partial x)|_i$. After a term-by-term comparison of these two equations, we are led to get the coefficients, shown in (33) and (34), as follows:

$$\alpha_1=0.875 \tag{35}$$

$$\beta_1=0.125128234159909 \tag{36}$$

$$\beta_2=-0.248717658400910 \tag{37}$$

$$\beta_3=0.000128234159909 \tag{38}$$

$$\gamma_1=-1.935961190081093 \tag{39}$$

$$\gamma_2=-0.060961190081093 \tag{40}$$

To eliminate the spurious oscillations in the vicinity of high gradient solutions, the ULTIMATE strategy proposed in [28] is employed.

5.2. Sixth-order accurate symplectic time-stepping scheme for the pure advection equation

Calculation of the level set equation is followed to approximate the remaining time derivative term shown in the ordinary differential equation for (6), where the spatial derivatives have been approximated in Section 5.1. The pure advection equation (6) has been well known to possess the following generalized enstrophies [23]:

$$C_n=\int \phi^n \mathrm{d}x\,\mathrm{d}y \tag{41}$$

where $n=0, 1, 2, \ldots$. Take $n=1$ as an example, $C_1=\int \phi\,\mathrm{d}x\,\mathrm{d}y=\Sigma\phi(\Delta x\Delta \mathrm{d}y)$ should be conserved exactly. Thanks to constant values of ρ_1, ρ_2 and, thus, $\rho_1+(\rho_2-\rho_1)\phi(\equiv\rho)$, the value $\int \rho\,\mathrm{d}x\,\mathrm{d}y$ will be also conserved.

Define the area enclosed by the set as $\Omega_c=\{(x, y): \phi(x, y)\geqslant c\}$, where c is 0.5 for the representation of free surface. Thanks to the existing Casimir, defined by Equation (41), holding at $n=0$, we are led to know that the following area function for the field variable ϕ with the magnitude larger than c is preserved [23]:

$$C_0(c)=\int_{\Omega_c} \mathrm{d}x\,\mathrm{d}y \tag{42}$$

This implies that the area (for the two-dimensional case) or the volume (for the three-dimensional case) enclosed by an interface, which is denoted by $\phi=c$, remains unchanged all the time. Development of an advection scheme for Equation (6) that possesses the conserved quantity $C_0(c)$ becomes therefore important in the prediction of interface in an incompressible fluid flow.

Equation (6) subjected to the constraint condition $\nabla\cdot\underline{u}=0$ is also known to have the following Hamiltonian [23]:

$$H=\frac{1}{2}\int_\Omega \psi\phi\,\mathrm{d}\Omega \tag{43}$$

where ψ denotes the stream function governed by $u=\partial\psi/\partial y$ and $v=-\partial\psi/\partial x$. Employment of a scheme that accommodates the above Hamiltonian property is also essential in the prediction of interface using the level set method [29].

For the purpose of preserving the long-time accurate Hamiltonian and Casimir properties embedded in Equation (6), the time derivative term will be discretized by the symplectic scheme. In this paper, the following sixth-order temporally accurate implicit symplectic Runge–Kutta scheme [30] will be employed to solve the ordinary differential equation.

DOI: 10.1002/fld

Given the time accurate solution ϕ^n at $t=n\Delta t$, we will calculate ϕ^{n+1} by marching the calculation by a time step Δt using the following iterative method. We start with the guessed values $\phi^{(i)}$ for ϕ^n, where $i=1\sim3$, and then calculate the values of $F^{(i)}$. This is followed by substituting $F^{(i)}(i=1\sim3)$ into the following three equations to get the updated values of $\phi^{(i)}(i=1\sim3)$.

$$\phi^{(1)}=\phi^n+\Delta t\left[\frac{5}{36}F^{(1)}+\left(\frac{2}{9}+\frac{2\widetilde{c}}{3}\right)F^{(2)}+\frac{5}{36}+\frac{\widetilde{c}}{3}\right)F^{(3)}\Bigg] \tag{44}$$

$$\phi^{(2)}=\phi^n+\Delta t\left[\left(\frac{5}{36}-\frac{5\widetilde{c}}{12}\right)F^{(1)}+\frac{2}{9}F^{(2)}+\left(\frac{5}{36}+\frac{5\widetilde{c}}{12}\right)F^{(3)}\right] \tag{45}$$

$$\phi^{(3)}=\phi^n+\Delta t\left[\left(\frac{5}{36}-\frac{\widetilde{c}}{3}\right)F^{(1)}+\left(\frac{2}{9}-\frac{2\widetilde{c}}{3}\right)F^{(2)}+\frac{5}{36}\right] \tag{46}$$

where $\widetilde{c}=\frac{1}{2}\sqrt{\frac{3}{5}}$. Note that $F^{(i)}(\equiv-\nabla\cdot(\underline{u}\phi^{(i)}))$, which is shown in the right-hand side of Equation (6), for $(i=1\sim3)$ represent the values of F evaluated, respectively, at $t=n+(\frac{1}{2}+\widetilde{c})\Delta t$, $t=n+\frac{1}{2}\Delta t$ and $t=n+(\frac{1}{2}-\widetilde{c})\Delta t$. Unless the difference of $\phi^{(i)}$ between two consecutive iterations becomes negligibly small, we continue the calculation of $F^{(i)}$ according to Equations (44)–(46). Upon reaching the user-specified tolerance, we can calculate the solution at the time $(n+1)\Delta t$ from the following equation:

$$\phi^{n+1}=\phi^n+\Delta t[\tfrac{5}{18}F^{(1)}+\tfrac{4}{9}F^{(2)}+\tfrac{5}{18}F^{(3)}] \tag{47}$$

6. VERIFICATION STUDIES

For the sake of assessment of the symplectic DRP scheme proposed for solving the level set equation, we defined below the computed error cast in its percentage form for the conserved quantities $C_n^{\text{Error}}=((C_n(t)-C_n(t=0))/C_n(t=0))\times100\%$ $(n=0,1)$ and $H^{\text{Error}}=((H(t)-H(t=0))/H(t=0))\times100\%$.

6.1. Rotation of a Gaussian profile in an inviscid flow

To verify the proposed fifth-order spatially accurate DRP advection scheme, the problem with the smooth Gaussian profile $e^{(-((x+3)/2^2)-(y+3)/2^2)}$ for Equation (5) will be investigated in $-1\leqslant x\leqslant1$ and $-1\leqslant y\leqslant1$ with the prescribed rotating velocity field $u=-2\pi y/9$ and $v=2\pi x/9$. The L_2 error norms predicted at different grids are given in Table I, from which the proposed method is justified and the rates of convergence are known from the results calculated at the times after 10 and 20 rotations.

6.2. Two-vortex flow in a box

The two-vortex problem is then investigated in a square domain, within which the velocity field is given by $u=-\sin^2(\pi x)\sin(2\pi y)$ and $v=\sin^2(\pi y)\sin(2\pi x)$. Two centers of the rotating velocity

Table I. The predicted L_2-error norms and the spatial rates of convergence (R.O.C.) after 10 and 20 rotations in the domains of three chosen meshes and at $\Delta t=\frac{1}{1000}$ for the rotating of a smooth Gaussian profile.

10 rotations			20 rotations		
Grids	L_2 error norms	R.O.C.	Grids	L_2 error norms	R.O.C.
20×20	1.5097E−002		20×20	2.0968E−002	
40×40	7.0508E−004	4.42	40×40	1.3297E−003	4.02
60×60	9.7930E−005	4.87	60×60	1.7779E−004	4.96

DOI: 10.1002/fld

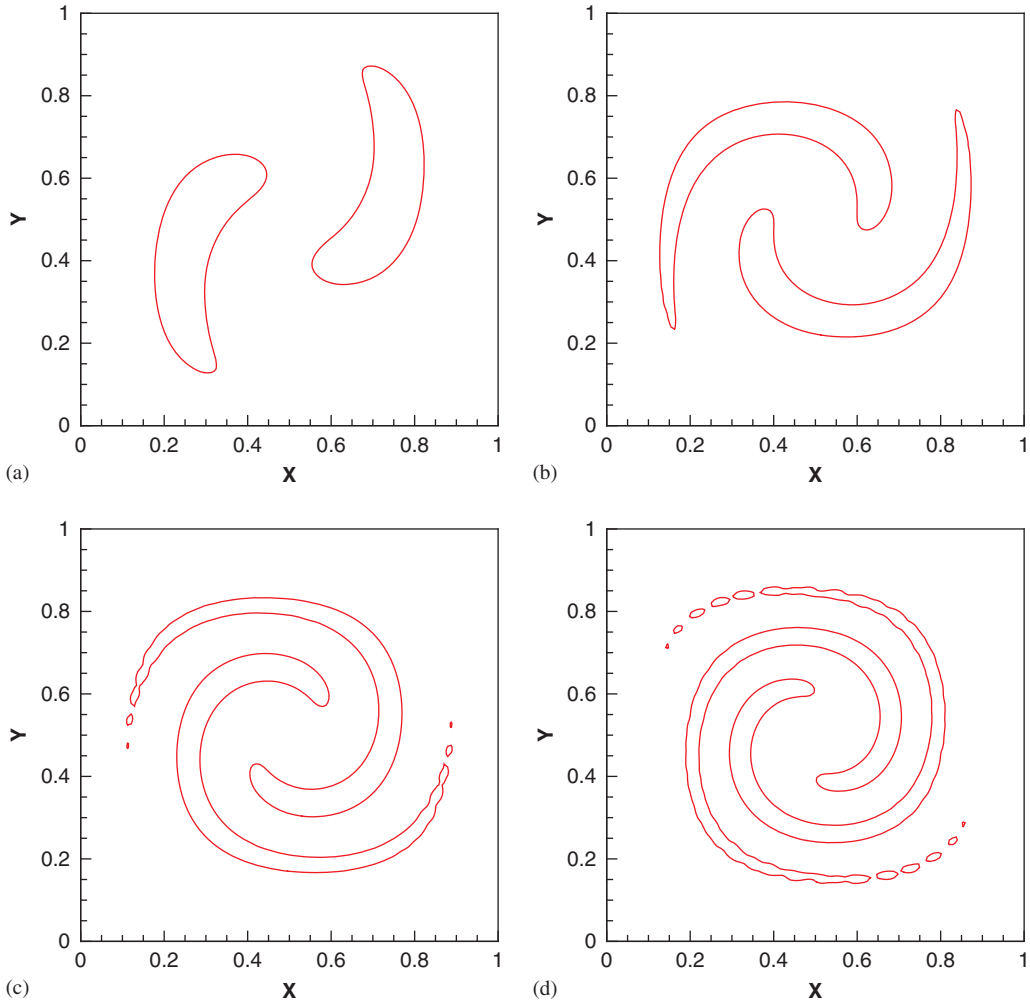

Figure 1. The predicted interfaces at the four chosen times in a domain of 120×120 grids: (a) $t = 0.4$; (b) $t = 0.8$; (c) $t = 1.2$; and (d) $t = 1.6$.

field, defined in a circle of radius 0.15, are located at $(0.5, 0.75)$ and $(0.5, 0.25)$. This test problem has a nonzero vorticity and will be solved at $\Delta t = \frac{1}{1000}$ in a domain of 120×120 and 240×240 grids. The predicted results plotted, respectively, in Figures 1 and 2 at $t = 0.4$, $t = 0.8$, $t = 1.2$ and $t = 1.6$ are seen to get distorted and form two long filamentary shapes owing to the specified stretching and tearing flow. We plot the predicted values of Casimir percentage error C_n^{Error} $(n = 0, 1)$ and Hamiltonian percentage error H^{Error} against time in Figure 3, from which the values of C_1^{Error}, C_2^{Error} and H^{Error} are all seen to conserve fairly well. To verify the proposed conservative spatially accurate DRP advection scheme, at a time $t = T$ $(T = 1.6)$ we reverse the flow field so that the exact solution at $t = 2T$ should be identical to the initial solution. For this reason, we plot Figure 4, which consists of the initial solution profile and the predicted solution profile at $t = 2T$. The predicted L_1 error norms at $t = 2T$ and the corresponding spatial rates of convergence are tabulated in Table II. Note that the convergence rate is determined from the computed error norms [17], defined by $\int_\Omega |\Phi_{\text{numerical}}(\underline{x}, 2T) - \Phi_{\text{exact}}(\underline{x}, t = 0)|/L \, \mathrm{d}\Omega$, where $L(= 0.3\pi)$ represents the circumference. We also plot the predicted values of Casimir percentage error C_n^{Error} $(n = 0, 1)$ and Hamiltonian percentage error H^{Error} against time in Figure 5. Our currently predicted vortex shape and mass conservation are seen to be better than those of Olsson *et al.* in [22].

DOI: 10.1002/fld

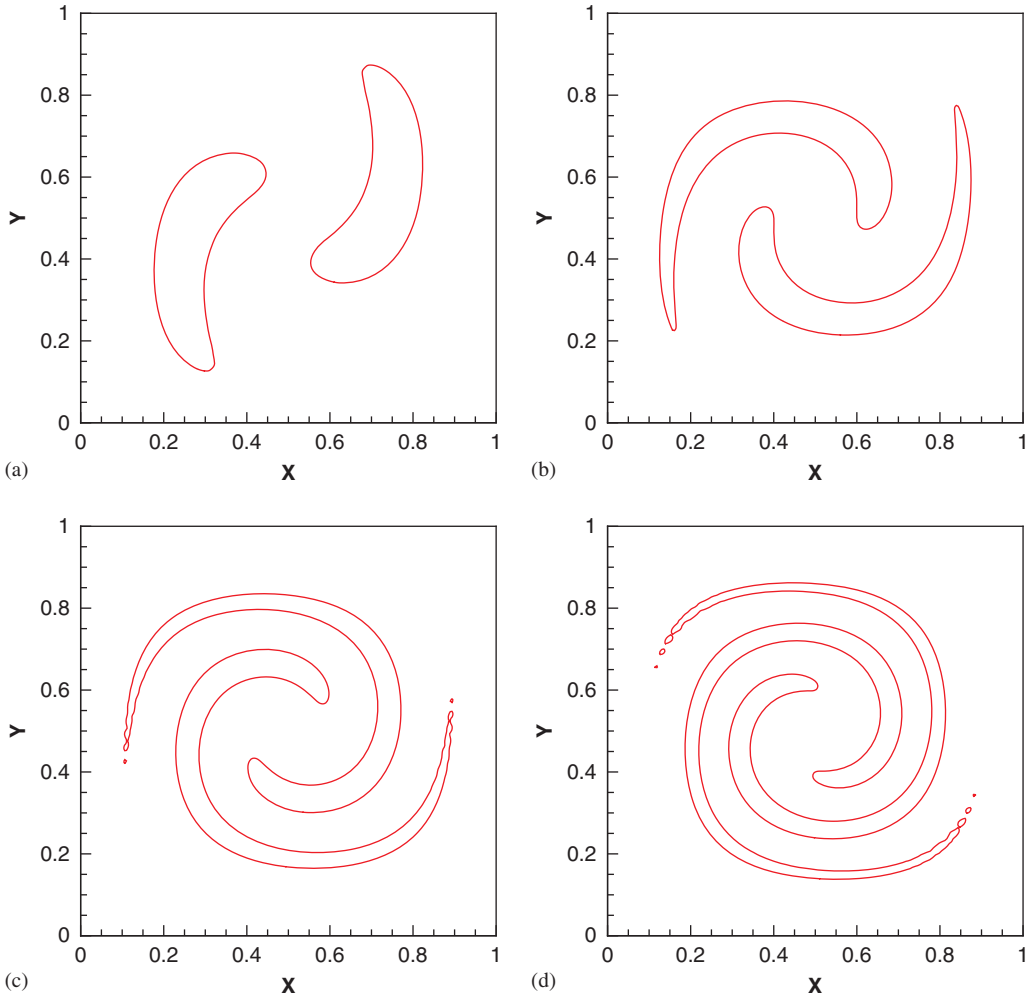

Figure 2. The predicted interfaces at the four chosen times in a domain of 240×240 grids: (a) $t = 0.4$; (b) $t = 0.8$; (c) $t = 1.2$; and (d) $t = 1.6$.

6.3. Rotation of a Zalesak's slotted disk

To verify the proposed spatially accurate DRP advection scheme with sharply varying solution, the initial profile of a notched disc type with the slot width of 15, which is rotated about the point at (50,75) in an inviscid flow with the velocity field given by $(u, v) = (\pi(50 - y)/314, \pi(x - 50)/314)$, will be considered [31, 32]. Calculation will be carried out in 100×100 and 200×200 grids to get the solutions at times after one and five revolutions. The computed solutions shown in Figures 6 and 7 were seen to be in good agreement with the exact (or initial) solution. The computed Casimir error C_n^{Error} $(n = 0, 1)$ and Hamiltonian error H^{Error} shown in Figure 8 at the time after the initial profile being rotated by five revolutions demonstrate that the conservative properties are indeed embedded in the approximated equation for the transport of level set function. The computed L_1 error norms and the corresponding spatial rates of convergence are tabulated in Table III. While our predicted results are superior to those predicted by S. P. van der Pijl *et al.* [31] in 100×100 and 200×200 grids, it is comparatively expensive to carry out the coupled compact calculation owing to the necessity of performing a triangular matrix calculation.

DOI: 10.1002/fld

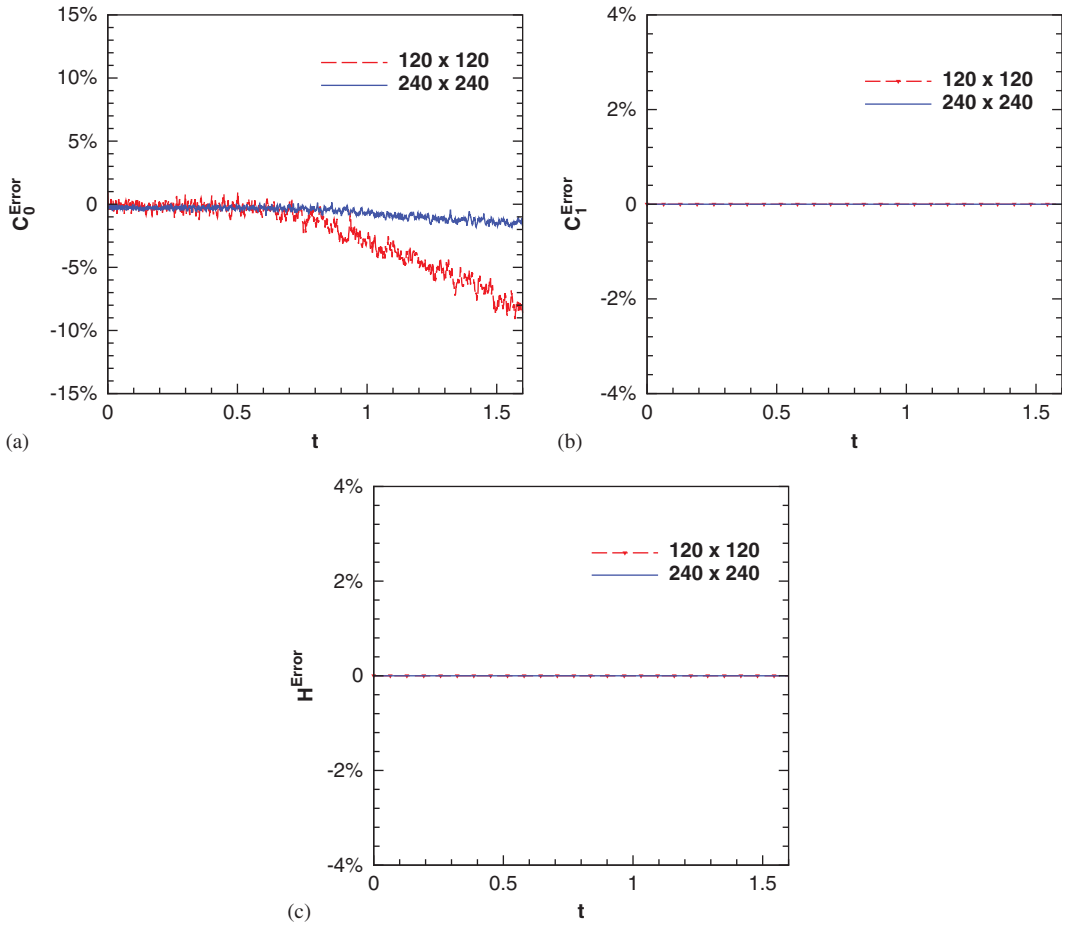

Figure 3. Comparison of three conserved quantities in percentage error form for the cases investigated in 120×120 and 240×240 grids: (a) C_0^{Error}; (b) C_1^{Error}; and (c) H^{Error}.

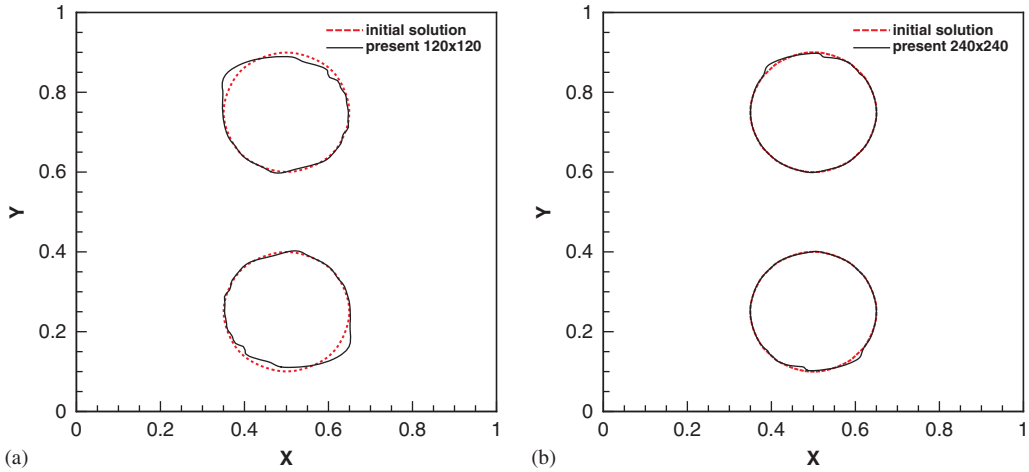

Figure 4. Comparison of the initial solution and the solution predicted at $t = 2T$ $(T = 1.6)$ in the two chosen grids: (a) 120×120 grids and (b) 240×240 grids.

DOI: 10.1002/fld

Table II. The predicted L_1 error norms at $t=2T$ and the spatial rates of convergence (R.O.C.), for the case with $T=1.6$, in the five chosen meshes and $\Delta t=\frac{1}{1000}$.

Grids	L_1 error norms	R.O.C.
40×40	7.560E−002	
60×60	4.752E−002	1.16
80×80	2.673E−002	2.00
120×120	1.188E−002	2.00
240×240	2.761E−003	2.10

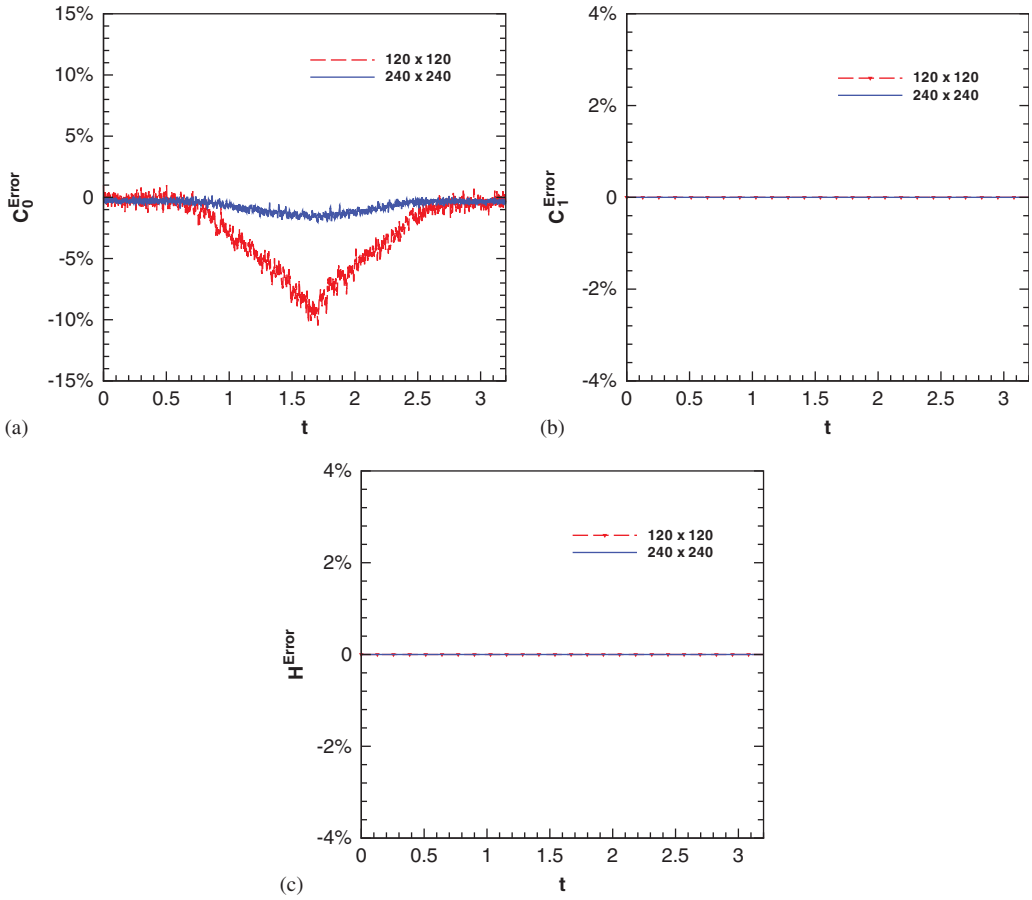

Figure 5. Comparison of three conserved quantities in percentage error form for the cases investigated in 120×120 and 240×240 grids: (a) C_0^{Error}; (b) C_1^{Error}; and (c) H^{Error}.

6.4. *Lid-driven cavity flow problem*

The flow driven by a constant upper lid velocity $u_{\text{lid}}(=1)$ in the square cavity is then investigated at $Re=100, 1000, 5000$ and 7500. The simulated grid-independent mid-plane velocity profiles for $u(0.5, y)$ and $v(x, 0.5)$ are plotted in Figure 9. Good agreement with the benchmark solution of Ghia [33] validates the proposed incompressible flow solver implemented in the two-dimensional non-staggered grids. The applicability of the proposed scheme to predict the incompressible fluid flow at high Reynolds numbers is therefore confirmed.

DOI: 10.1002/fld

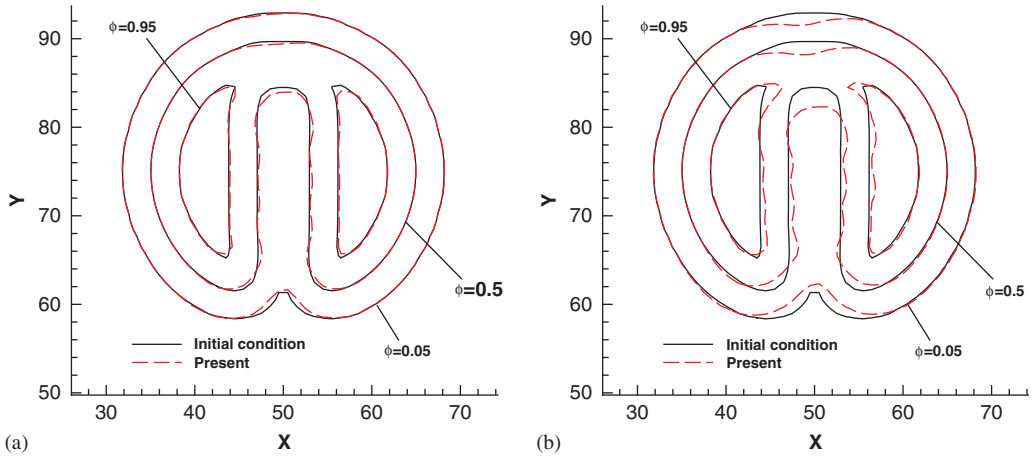

Figure 6. The predicted solutions for ϕ in a mesh of 100×100 nodal points using the proposed two-step symplectic DRP scheme: (a) after one rotation and (b) after five rotations.

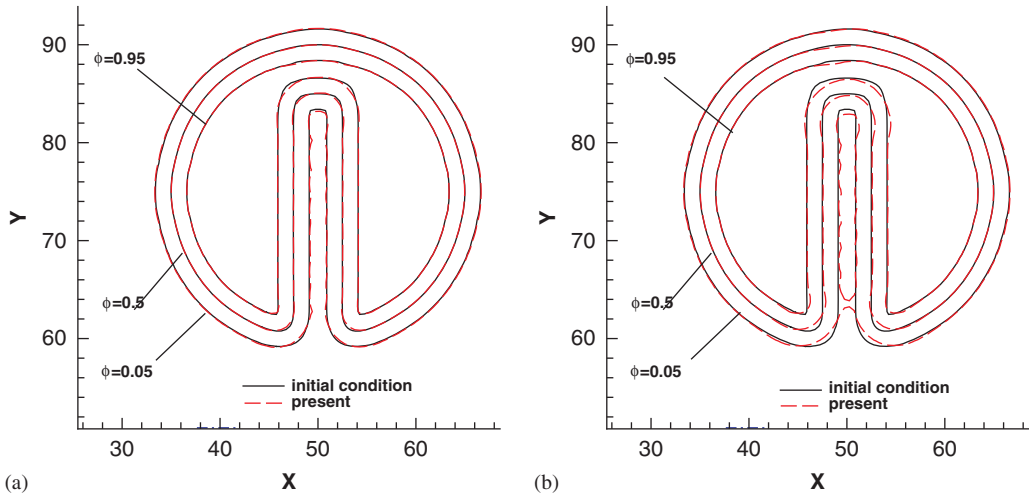

Figure 7. The predicted solutions for ϕ in a mesh of 200×200 nodal points using the proposed two-step symplectic DRP scheme: (a) after one rotation and (b) after five rotations.

7. NUMERICAL RESULTS

After verifying the advection scheme and the incompressible flow solver, we are proceeded to justify the proposed conservative level set method by virtue of the following five problems, which all involve predicting the time-varying interfaces. The first test problem, known as the dam break problem, is chosen to demonstrate the ability of applying the proposed interface capturing method to solve the problem without taking the surface tension into account. Another well-known Rayleigh–Taylor problem is also solved in this study for the validation sake. The third and fourth simulations are known as the air bubble rising in two- and three-dimensional water tanks, and the fifth problem simulates the droplet falling into water, respectively. Since surface tension along the gas/water interface has an ineligible impact on the time-evolving air bubble or water droplet interface, this interfacial force will be considered in both cases.

DOI: 10.1002/fld

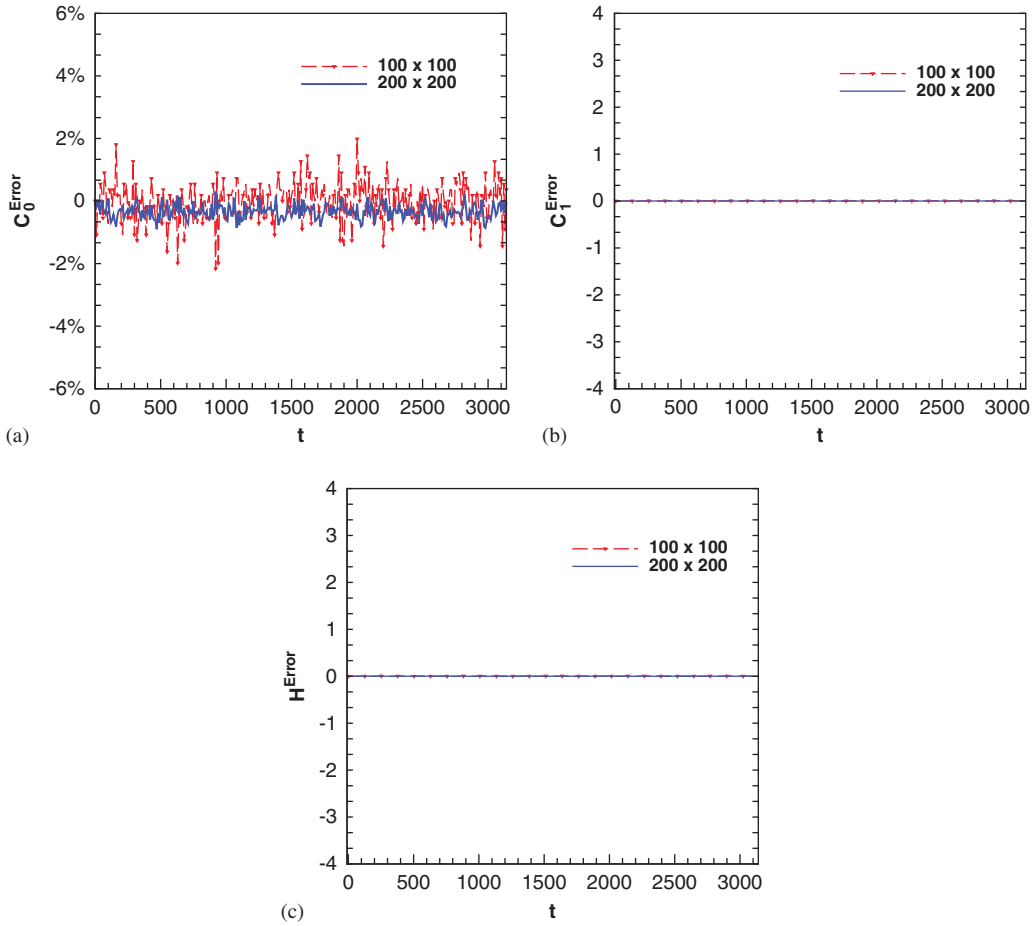

Figure 8. Comparison of three conserved quantities in percentage error form for the cases investigated in 100×100 and 200×200 grids: (a) C_0^{Error}; (b) C_1^{Error}; and (c) H^{Error}.

Table III. The predicted L_1 error norms and the spatial rates of convergence (R.O.C.) after one and five revolutions in the four chosen meshes and $\Delta t=\frac{1}{2}$.

1 Revolution			5 Revolutions		
Grids	L_1 error norms	R.O.C.	Grids	L_1 error norms	R.O.C.
100×100	0.286		100×100	0.325	
150×150	0.122	2.11	150×150	0.138	2.12
200×200	5.163E−002	2.25	200×200	6.835E−002	2.44
300×300	2.705E−002	1.29	300×300	3.244E−002	1.84

7.1. Interface prediction without surface tension

7.1.1. Dam break problem. The first problem without taking surface tension into account simulates a sudden collapse of a rectangular water column onto a planar surface. This classical problem, known as the dam break problem, has been frequently employed to validate the computer code developed for the prediction of free surface. In addition to the hydraulic importance of this problem, experimental [34] and numerical results [35] are both available for properly making a direct comparison study.

DOI: 10.1002/fld

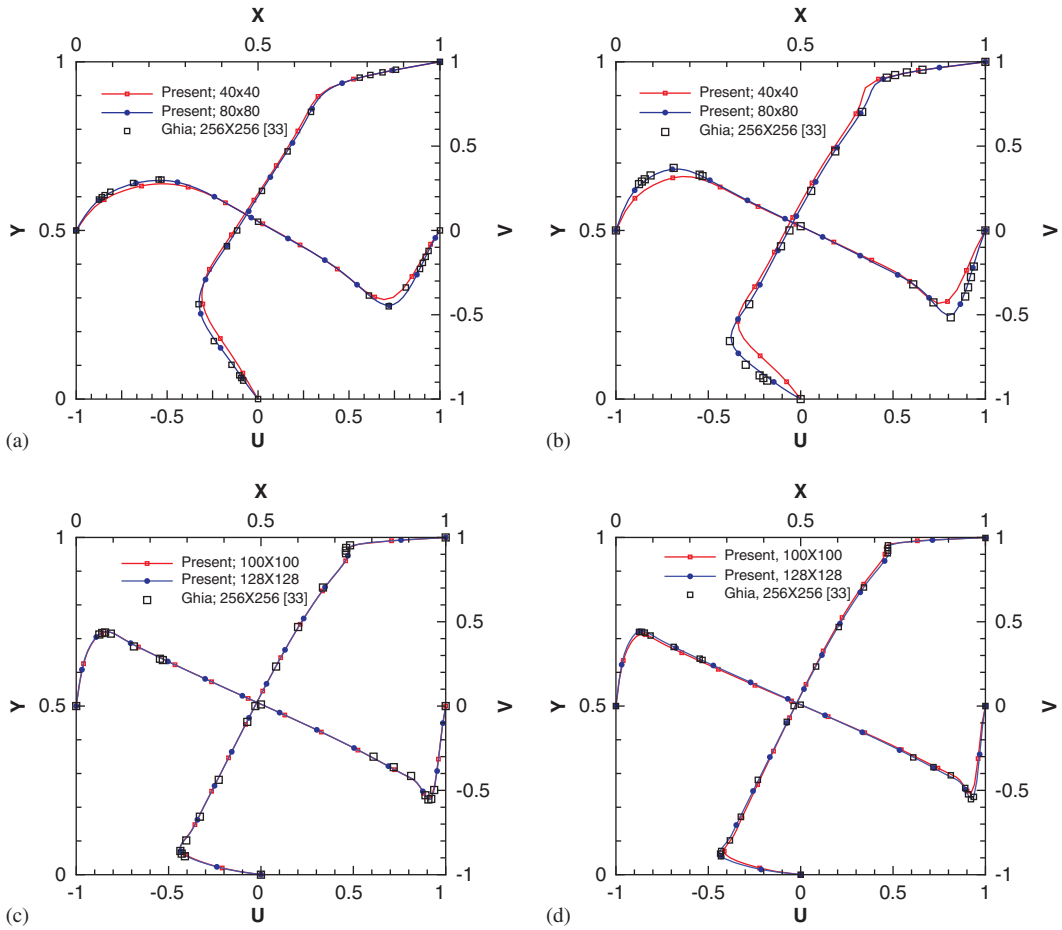

Figure 9. Comparison of the predicted mid-plane velocity profiles for the case investigated at four Reynolds numbers: (a) $Re=100$; (b) $Re=1000$; (c) $Re=5000$; and (d) $Re=7500$.

In the current calculation, the fluid properties are assumed to be the same as those studied in [35]. The results will be predicted at $Re=42\,792$ in the domain containing 300×75 nodal points. The predicted heights of the collapsed water column are plotted against the dimensionless time, defined in [35], for the comparison sake. Good agreement with the experimental result given in [34] is clearly demonstrated in Figure 10 for the simulated surge front location and the water column height. The predicted time-evolving free surfaces in Figure 11 are also compared favorably with the finite element solutions of Kelecy and Pletcher [35].

For making a further indirect verification of the predicted results, we plot the values of Casimir errors C_n^{Error} $(n=0,1)$ against time in Figure 12. Both of them are seen to be well conserved in the sense that both mass and area remain almost identical to their corresponding values prescribed at the initial time.

7.1.2. Rayleigh–Taylor problem. Rayleigh–Taylor instability arises due to the penetration of a heavy fluid into a light fluid along the direction of gravity. Such a phenomenon has been observed in many scientific and environmental fields and has, therefore, been intensively studied [8]. Two incompressible fluids with the densities and viscosities given by $\rho_h=1$, $\rho_l=\frac{1}{3}$, $\mu_h=1$, and $\mu_l=1$ will be simulated in the rectangle of $0\leqslant x\leqslant1$, $0\leqslant y\leqslant4$. The initial condition is given by $y(x)=2.0+0.1\cos(2\pi x)$ and the Reynolds number is 3000.

According to the referenced paper [8], we carry out the current simulation without considering surface tension for a fluid flow starting from rest in the domain where free slip boundary condition

DOI: 10.1002/fld

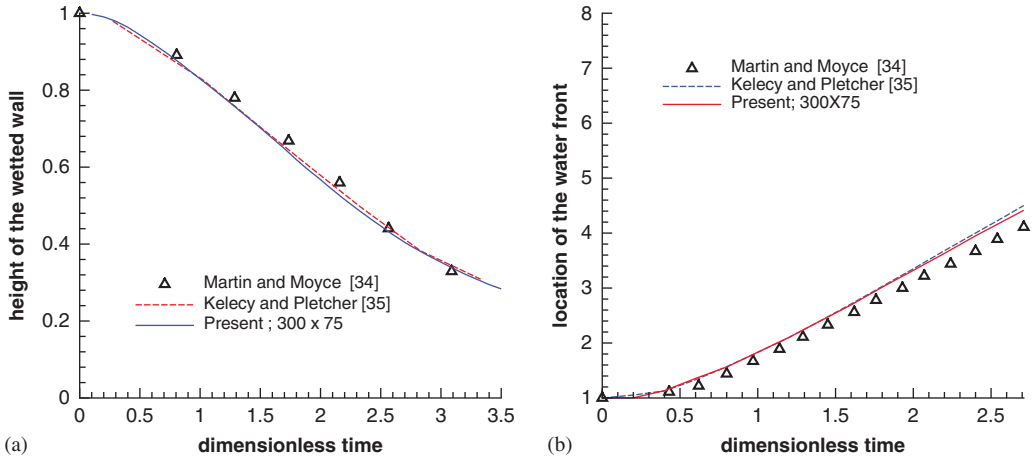

Figure 10. Comparison of the predicted surge front location and the water column height with the experimental data: (a) height of the wetted wall and (b) location of the water front.

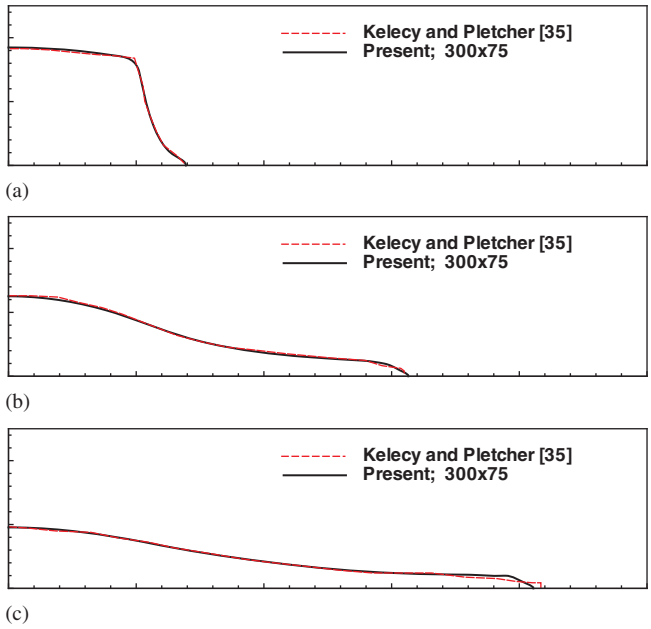

Figure 11. Comparison of the predicted free surfaces at the three chosen times for the dam-break problem investigated in 300×75 grids: (a) $t = 0.6$; (b) $t = 1.8$; and (c) $t = 2.4$.

and non-slip boundary condition are imposed at the two vertical walls and at the horizontal top/bottom walls, respectively. The predicted interface plotted in Figure 13 and the Casimir errors C_n^{Error} $(n = 0, 1)$ plotted in Figure 14 justify again the proposed two-step level set method and the spatial/temporal discretization schemes.

7.2. *Interface prediction with surface tension*

7.2.1. Two-dimensional rising bubble in a partially filled container. The time-evolving interface problem where surface tension needs to be taken into account is then investigated. The problem under current investigation analyzes the evolution of a stationary bubble, that is driven by surface tension, in a partially filled container. This container is partially filled with the viscous fluid of height 7.0 and width 7.0.

DOI: 10.1002/fld

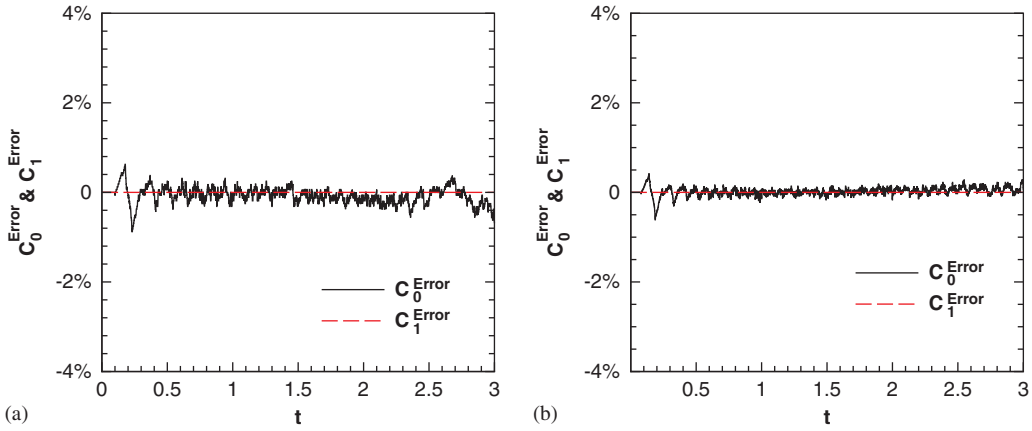

Figure 12. The predicted Casimir percentage errors ($n = 0, 1$), which are plotted against the dimensionless time for the cases carried out in two chosen grids: (a) 200×50 grids and (b) 300×75 grids.

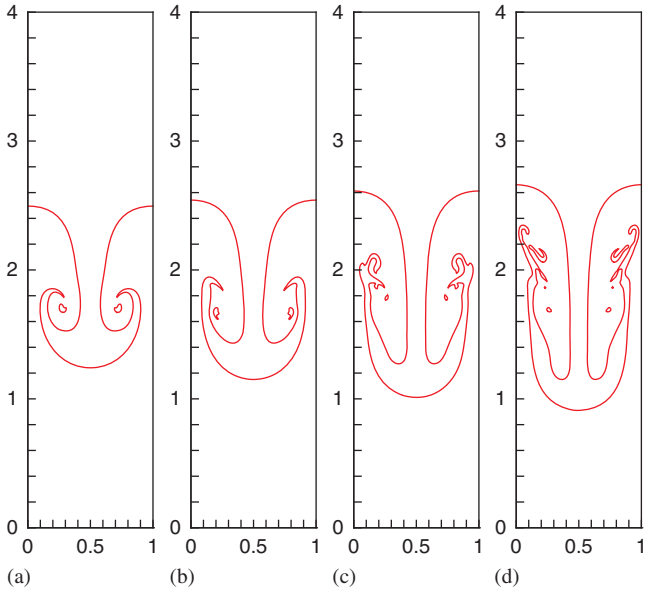

Figure 13. The predicted time-evolving interfaces at the four chosen times for the Rayleigh–Taylor problem investigated in 100×400 grids: (a) $t = 1.5$; (b) $t = 1.75$; (c) $t = 2.0$; and (d) $t = 2.5$.

The fluid–gas density and viscosity ratios are specified, respectively, as $\rho_l/\rho_g = 1000$ and $\mu_l/\mu_g = 100$. The subscripts l and g correspond to the fluid surrounding the air bubble and the fluid inside the air bubble, respectively. Initially, the bubble center is stationarily located at $(3.5, 1.5)$ in the water container, which is at rest everywhere. As usual, no-slip conditions are specified along the horizontal and vertical walls.

Since surface tension is essential in the course of bubble rising, surface tension effect will be investigated at $Re = 100$, $We = 200$ and $Fr = 1$ where Re, We and Fr are denoted as the Reynolds number, Weber number and Froude number, respectively. In Figure 15 the predicted free surface is plotted in 180×180 and 240×240 nodal points. Besides the good agreement between the predicted interfaces, Figures 16(a) and (b) show also the excellent preservation properties embedded in the Casimir errors C_n^{Error} $(n = 0, 1)$.

DOI: 10.1002/fld

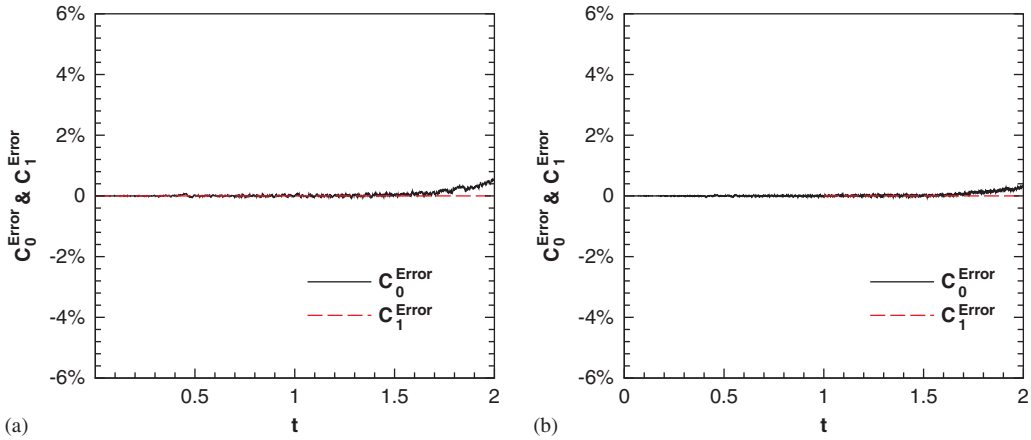

Figure 14. The predicted Casimir percentage errors ($n = 0, 1$), which are plotted against the dimensionless time for the cases carried out in the two chosen grids: (a) 100×400 grids and (b) 150×600 grids.

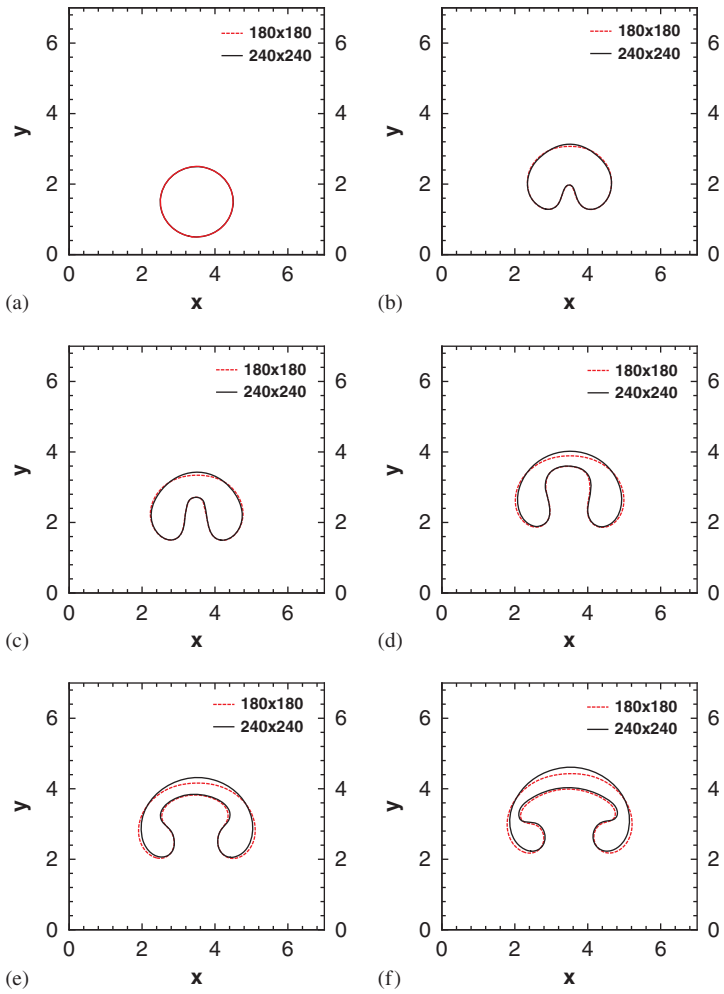

Figure 15. The predicted time-evolving interfaces at the four chosen times for the bubble rising problem in 180×180 and 240×240 grids: (a) $t = 0.0$; (b) $t = 1.5$; (c) $t = 2.0$; (d) $t = 3.0$; (e) $t = 3.5$; and (f) $t = 4.0$.

DOI: 10.1002/fld

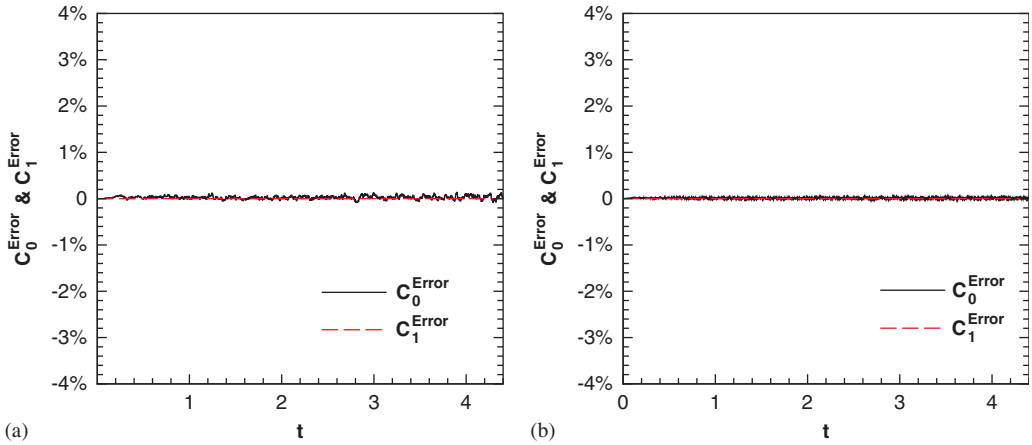

Figure 16. The predicted Casimir percentage errors ($n=0, 1$), which are plotted against the dimensionless time for the cases carried out in the two chosen grids: (a) 180×180 grids and (b) 240×240 grids.

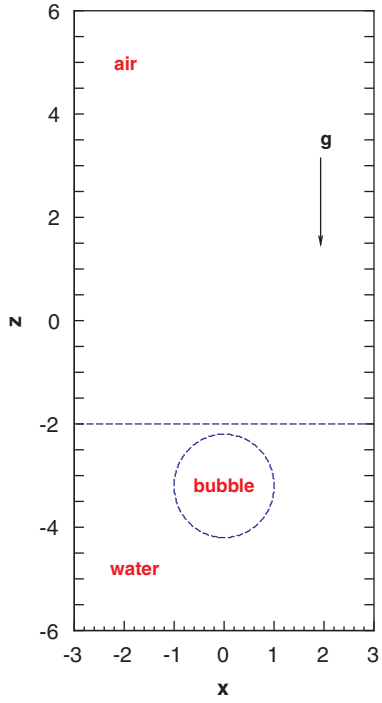

Figure 17. Schematic of the initial bubble location with its centroid at $(0, -3.2)$ in the container, which is defined in $-3\leqslant x\leqslant 3, -6\leqslant z\leqslant 6$ and partially filled with the water. Note that the initial free surface is at $z=-2$.

7.2.2. Three-dimensional bubble rising problem. The time-evolving interface problem is also investigated in the three-dimensional rectangular box of lengths 6, 6 and 12 ($-3\leqslant x\leqslant -3$, $-3\leqslant y\leqslant -3, -6\leqslant z\leqslant -6$), which is uniformly discretized to yield a mesh of $60\times60\times120$ nodal points. Initially, a spherical bubble centered at $(x, y, z)=(0, 0, -3.2)$ with the unit radius, schematic in Figure 17 (2D cutting at $y=0$), is released below the free surface. The fluid–gas density and viscosity ratios are specified, respectively, at $\rho_l/\rho_g=1000$ and $\mu_l/\mu_g=100$. As usual, no-slip conditions are specified along the walls.

DOI: 10.1002/fld

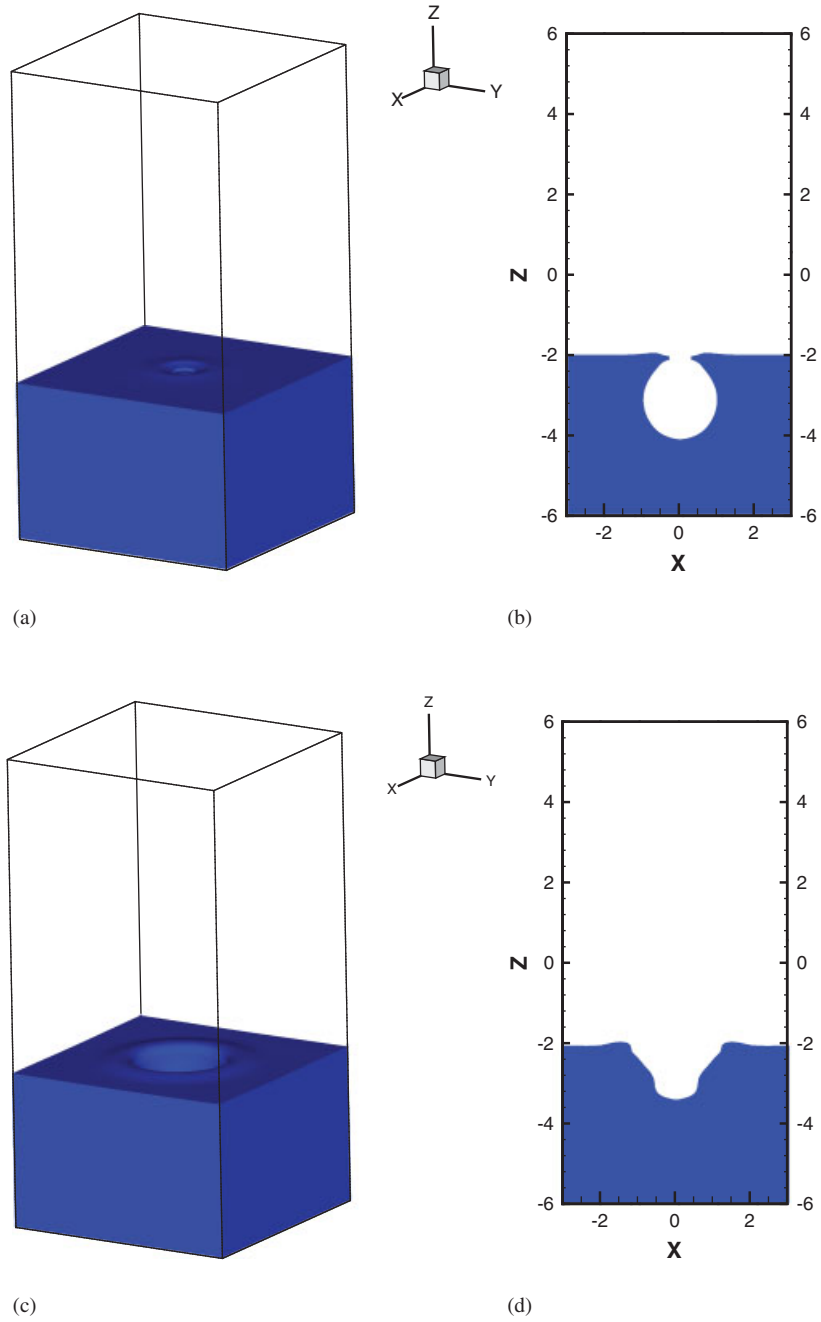

Figure 18. The predicted $3D$ free surfaces (in (a), (c), (e), (g)) and their corresponding $2D$ cutting free surfaces ($y=0$) (in (b), (d), (f), (h)) at the four chosen times for the bubble rising problem investigated in $60\times60\times120$ grids: (a),(b) $t=0.2$; (c),(d) $t=0.6$; (e),(f) $t=0.74$; and (g),(h) $t=1.0$.

Since surface tension will be generated during bubble rising, such an effect will be investigated at $Re=474$, $We=1$ and $Fr=0.64$. In Figure 18, the predicted 2D and 3D free surfaces and bubble interfaces are plotted at the four chosen times. As before, the excellent preserving properties in view of the predicted Casimir percentage errors C_n^{Error} ($n=0, 1$) are shown in Figure 19.

7.2.3. Droplet falling in water. A water droplet falling through the air and hitting on an initially planar free surface will be investigated in this study. In the two-dimensional rectangular box of

DOI: 10.1002/fld

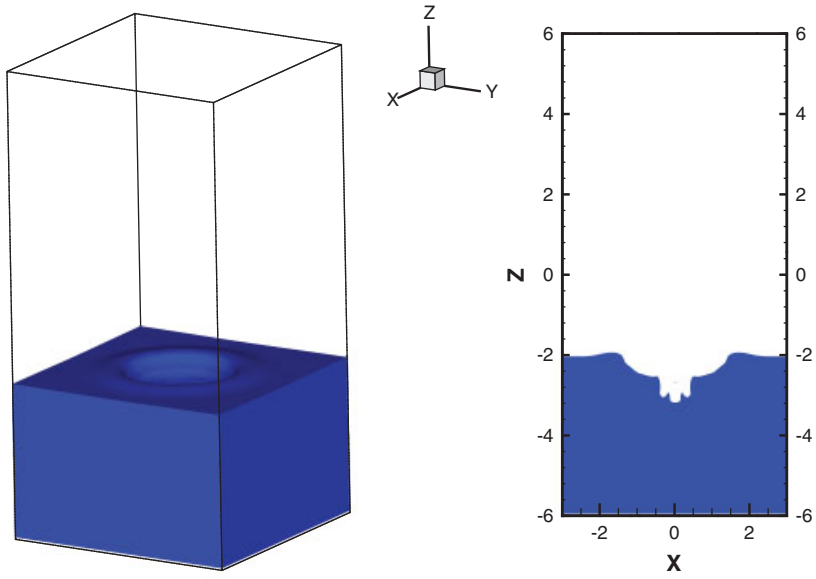

(e) (f)

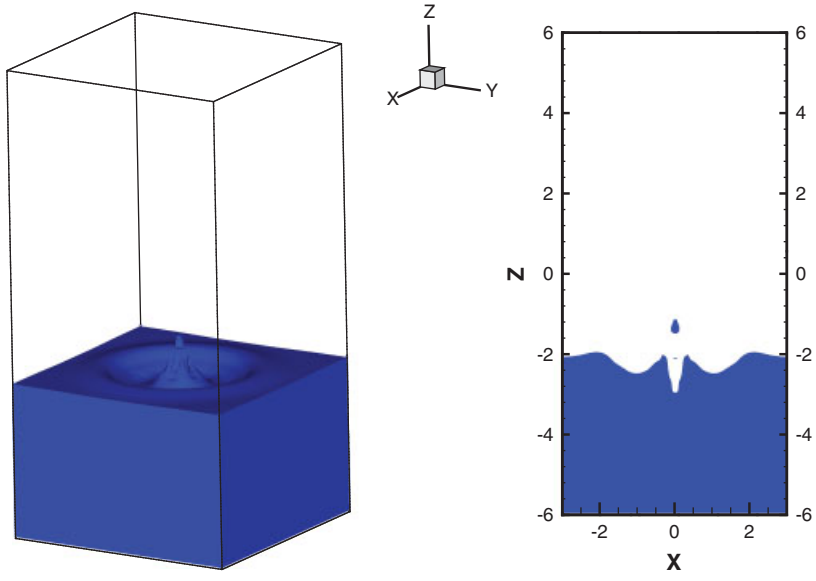

(g) (h)

Figure 18. *Continued*.

lengths 4 and 8 ($0 \leqslant x \leqslant 4, 0 \leqslant y \leqslant 8$), at $t = 0$ the semicircle droplet center is stationarily located at $(0.0, 5.0)$ and the container is partially filled with the viscous fluid of width $4(0 \leqslant x \leqslant 4)$ and height $4(0 \leqslant y \leqslant 4)$. The density and viscosity ratios are specified, respectively, as $\rho_l/\rho_g = 816$ and $\mu_l/\mu_g = 71$. Since the water droplet is accelerated initially from $t = 0$ with a fictitious gravitational force $1/Fr^2 = \frac{1}{2}$, three dimensionless parameters for characterizing this flow motion are chosen as $Fr = \sqrt{2}$ (in the time range of $0 < t \leqslant 2$), $Fr = 1633$ (in the time range of $2 < t \leqslant 7$), $Re = 3518$, and $We = 220$. No-slip conditions are specified along the horizontal and right vertical walls, slip condition is specified along the left vertical wall.

DOI: 10.1002/fld

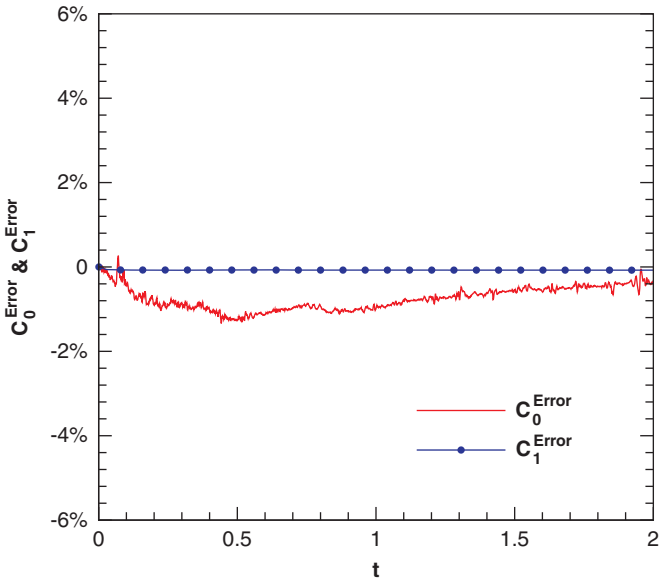

Figure 19. The predicted Casimir percentage errors ($n = 0,\ 1$), which are plotted against the dimensionless time for the case carried out in $60 \times 60 \times 120$ grids.

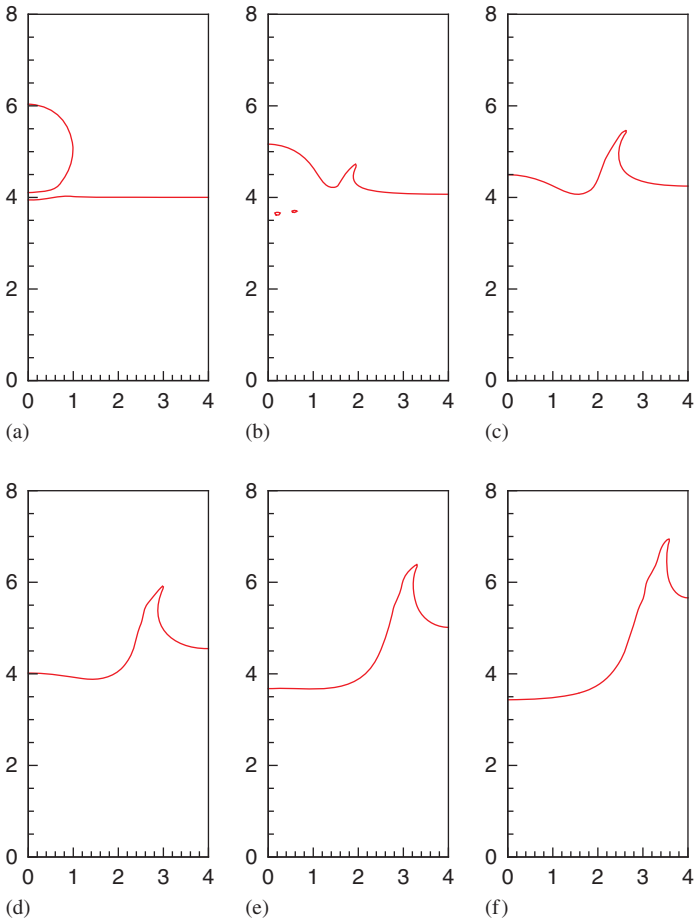

Figure 20. The predicted time-evolving interfaces at the six chosen times for the droplet falling problem investigated in 100×200 grids: (a) $t = 2.0$; (b) $t = 3.0$; (c) $t = 4.0$; (d) $t = 5.0$; (e) $t = 6.0$; and (f) $t = 7.0$.

DOI: 10.1002/fld

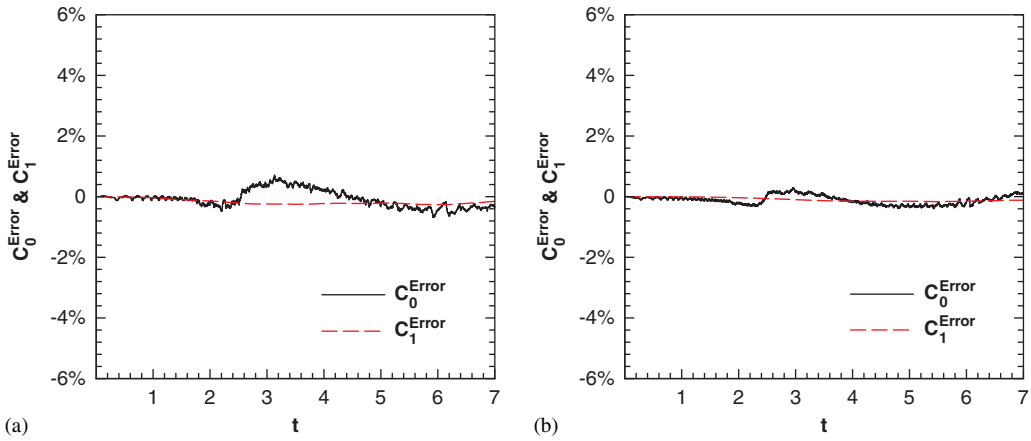

Figure 21. The predicted Casimir percentage errors ($n=0, 1$), which are plotted against the dimensionless time for the cases carried out in the two chosen grids. (a) 60×120 grids; (b) 100×200 grids.

This problem will be solved at $\Delta t=\frac{1}{1000}$ in a domain of 100×200 grids. The predicted time-evolving droplet interface and free surface are plotted in Figure 20. Note that the interface with $\phi=0.5$ is plotted at the dimensionless times $t=2.0$, $t=3.0$, $t=4.0$, $t=5.0$, $t=6.0$ and $t=7.0$. As Figure 21(a) and (b) shows, the Casimir percentage errors C_n^{Error} ($n=0, 1$) remain fairly well in the case taking into account the surface tension effect.

8. CONCLUDING REMARKS

A dispersion-relation-preserving advection scheme, formulated within the framework of coupled compact scheme, for approximating the incompressible two-phase flow equations in two dimensions by conservative level set method is developed in non-staggered grids. The present conservative level set method is split into the equation, known as the conventional level set method for the advection of level set function, and the nonlinear inhomogeneous equation with the inclusion of nonlinear flux term to compress the interface profile. Since the area within each contour of the level set function is preserved, we employ the symplectic time-stepping scheme to approximate the time derivative term shown in the first-step of the modified level set method so as to ensure the area-preserving property. The proposed spatial/temporal scheme with the respective accuracy orders of fifth and sixth has been used to solve three pure advection problems to demonstrate that both Hamiltonian and Casimir conservation properties are indeed embedded in the discrete equation. Also, the chosen five benchmark problems with/without consideration of surface tension have been numerically investigated with success.

ACKNOWLEDGEMENTS

This work was supported by the National Science Council of Republic of China under the Grants NSC-94-2611-E-002-021, NSC-94-2745-P-002-002 and CQSE project 97R0066-69.

REFERENCES

1. Sethian JA, Adalsteinsson D. An overview of level set methods for etching, deposition and lithography development. *IEEE Transactions on Semiconductor Manufacturing* 1997; **10**(1):167–184.
2. Anderson CR. A vortex method for flows with slight density variations. *Journal of Computational Physics* 1985; **61**(3):417–444.
3. Boultone-Stone JM, Blake JR. Gas bubbles bursting at a free surface. *Journal of Fluid Mechanics* 1993; **254**:437–466.

DOI: 10.1002/fld

4. Hirt CW, Nichols BD. Volume of fluid method (VOF) for the dynamics of free boundaries. *Journal of Computational Physics* 1981; **39**:201–225.
5. Unverdi S, Tryggvason G. A front-tracking method for viscous, incompressible, multi-fluid flows. *Journal of Computational Physics* 1992; **100**:25–37.
6. Badalassi VE, Ceniceros HD, Banerjee S. Computation of multiphase systems with phase field models. *Journal of Computational Physics* 2003; **190**:371–397.
7. Kim J. A continuous surface tension force formulation for diffuse-interface models. *Journal of Computational Physics* 2005; **204**:784–804.
8. Ding H, Spelt PDM, Shu C. Diffuse interface model for incompressible two-phase flows with large density ratios. *Journal of Computational Physics* 2007; **226**:2078–2095.
9. Sethian JA, Smereka P. Level set methods for fluid interfaces. *Annual Review of Fluid Mechanics* 2003; **35**: 341–372.
10. Hirt CW, Amsden AA, Cook JL. An arbitrary Lagrangian–Eulerian computing method for all flow speeds. *Journal of Computational Physics* 1997; **135**(2):203–216.
11. Harlow F, Welch J. Volume tracking methods for interfacial flow calculations. *Physics of Fluids* 1965; **8**:21–82.
12. Osher S, Sethian JA. Fronts propagating with curvature dependent speed: algorithms based on Hamilton–Jacobi formulation. *Journal of Computational Physics* 1988; **79**:12–49.
13. Marchandise E, Remacle JF, Chevaugeon N. A quadrature-free discontinuous Galerkin method for the level set equation. *Journal of Computational Physics* 2006; **212**:338–357.
14. Thomas PD, Lombard CK. Geometric conservation law and its application to flow computations on moving grids. *AIAA Journal* 1979; **17**(10):1030–1037.
15. Sheu TWH, Chen YH. Numerical study of flow field induced by a locomotive fish in the moving meshes. *International Journal for Numerical Methods in Engineering* 2007; **69**:2247–2263.
16. Enright D, Fedkiw R, Ferziger J, Mitchell I. A hybrid particle level set method for improved interface capturings. *Journal of Computational Physics* 2002; **183**:83–116.
17. Sussman M, Fatermi E, Smereka P, Osher S. An improved level set method for incompressible two-fluid flows. *Computers and Fluids* 1988; **127**:663–680.
18. Sussman M, Puckett E. A coupled level set and volume-of-fluid method for computing 3D and axisymmetric incompressible two-phase flow. *Journal of Computational Physics* 2000; **162**:301–337.
19. Strain J. Tree methods for moving interfaces. *Journal of Computational Physics* 1999; **151**:616–648.
20. Osher S, Fedkiw R. *Level Set Methods and Dynamic Implicit Surfaces*. Springer: Berlin, 2003.
21. Sethian JA. *Level Set Methods and Fast Marching Method*. Cambridge University Press: Cambridge, 2003.
22. Olsson E, Kreiss G. A conservative level set method for two phase flow. *Journal of Computational Physics* 2005; **210**:225–246.
23. McLachlan RI. Area preservation in computational fluid dynamics. *Physics Letters A* 1999; **264**:36–44.
24. Chu PC, Fan C. A three-point combined compact difference scheme. *Journal of Computational Physics* 1998; **140**:370–399.
25. Tam CKW, Webb JC. Dispersion-relation-preserving finite difference schemes for computational acoustics. *Journal of Computational Physics* 1993; **107**:262–281.
26. Ladyzhenskaya OA. *The Mathematical Theory of Viscous Incompressible Flow*. Gordon and Breach: New York, 1969.
27. Sheu TWH, Chiu PH. A divergence-free-condition compensated method for incompressible Navier–Stokes equations. *Computer Methods in Applied Mechanics and Engineering* 2007; **196**:4479–4494.
28. Leonard BP. The ULTIMATE conservative difference scheme. *Computer Methods in Applied Mechanics and Engineering* 1991; **88**:17–74.
29. Sussman M, Smereka P, Osher S. A level set approach for computing solution to incompressible two-phase flow. *Journal of Computational Physics* 1994; **114**:146–159.
30. Oevel W, Sofroniou W. *Symplectic Runge–Kutta Schemes II*: *Classification of Symplectic Method*, University of Paderborn, Germany, 1997.
31. Van der Pijl SP, Segal A, Vuik C, Wesseling P. A mass-conserving level-set method for modelling of multi-phase flows. *International Journal for Numerical Methods in Fluids* 2005; **47**:339–361.
32. Zalesak ST. Fully multidimensional flux corrected transport algorithms for fluids. *Journal of Computational Physics* 1979; **31**:335–362.
33. Ghia U, Ghia KN, Shin CT. High-*Re* solutions for incompressible flow using the Navier–Stokes equations and a multigrid method. *Journal of Computational Physics* 1982; **48**:387–411.
34. Martin J, Moyce W. An experimental study of the collapse of liquid columns on a rigid horizontal plane. *Philosophical Transactions* 1952; **224**:312–324.
35. Kelecy FJ, Pletcher RH. The development of a free surface capturing approach for multidimensional free surface flows in closed containers. *Journal of Computational Physics* 1997; **138**:939–980.

DOI: 10.1002/fld